12-20-2015

Thermal Transport and Melt Pool Geometry in Metallic Powder Bed Additive Manufacturing Processes for Various Novel Engineering Materials

John P. Romano II
john.romano@uconn.edu

Thermal Transport and Melt Pool Geometry in Metallic Powder Bed Additive Manufacturing Processes for Various Novel Engineering Materials

John Peter Romano II

B.S., University of Connecticut, 2014

A Thesis

Submitted in Partial Fulfillment of the

Requirements for the Degree of

Master of Science

At the

University of Connecticut

2015

APPROVAL PAGE

Master of Science Thesis

Thermal Transport and Melt Pool Geometry in Metallic Powder Bed Additive Manufacturing Processes for Various Novel Engineering Materials

Presented by

John Peter Romano II, B.S.

Major Advisor_____

Dr. Leila Ladani

Associate Advisor_____

Dr. Jiong Tang

Associate Advisor_____

Dr. Brice Cassenti

University of Connecticut

2015

Acknowledgements

The following made significant contributions to the success of this thesis. I would not have been able to accomplish this project without their help and support.

Pratt & Whitney, for financial support of the work in this thesis, and all members of the project for their expertise and guidance;

Dr. Leila Ladani, my advisor, who patiently guided me and motivated me throughout the past year and a half of working in the Mechanics, Materials and Manufacturing Laboratory;

Magda Sadowski for helping me work through various modeling issues and being someone I can bounce ideas off of;

Nicole Romano, my sister, for the constant encouragement and dining hall food;

Dr. Jiong Tang and Dr. Brice Cassenti, my advisory committee;

and to my lab mates, friends, and family for their encouragement and assistance throughout the entire course of this project.

Table of Contents

List of Figures

List of Tables

Thermal Transport and Melt Pool Geometry in Metallic Powder Bed Additive Manufacturing Processes for Various Novel Engineering Materials

Abstract

by

John Peter Romano II

Laser and electron beam powder bed melting additive technologies are being rapidly adapted by industry. These technologies rely on the ability to produce defect free parts through a delicate control of the process. However, this process has not been attempted or has failed for many common metallic materials such as Aluminum. The objective of this thesis was to understand the thermal transport phenomenon in electron and laser beam powder melting technology through simulation and experiments and determine the suitable range of parameters that can be used for common metallic materials. A finite element model was developed using ANSYS APDL to explore thermal transport and phase change behavior in metallic powder bed additive manufacturing processes. To explore a broad base of novel engineering materials, simulations were run in Ti6Al4V, Inconel 718, Stainless Steel 316L and Al7075 in both selective laser melting and electron beam melting scenarios. Comparison of the four materials in each process showed that it is very challenging to develop and maintain melt pools in aluminum while melt pools are broad and robust in Inconel and titanium, even when subjected to much lower energy densities. Titanium and Inconel were also shown to have larger melt pools and shallower thermal gradients.

Effective powder thermal conductivity was used to encapsulate all modes of heat transfer occurring at the inter-particle level and allow the use of macro-level size scale parameters for the finite element analysis. Additionally, an effective liquid conductivity is derived to capture the effects of fluid dynamics and advective transport effects within the melt pool and more accurately predict melt pool geometries without the need for coupled computational fluid dynamics analyses governing the melt pool. Experimental validations in Inconel at beam powers of 150W, 200W and 300W were performed. Inclusion of effective liquid conductivity resulting in simulation results becoming an average of 40% closer to experimental melt pool measurements

CHAPTER 1 Introduction

1.1 History of Additive Manufacturing Processes

Additive manufacturing (AM) represents a group of processes in which parts are built by fusing material layer upon layer. This technology is contrary to traditional, subtractive manufacturing technologies in which parts are formed from larger working pieces by removing extraneous material. Historically, AM was seen mainly as a rapid prototyping tool since it allows designers to quickly develop their prototypes and test their parts. AM was not considered a viable method for high volume production runs of parts. There are a variety of factors that play a role in this perception including: limited build volume, long build times, costly materials, and lack of understanding of material properties from additively built parts. AM encompasses a wide variety of processes working in a wide variety of media.

Over the past 30 years, the fields of AM, rapid tooling, and rapid prototyping has been blossoming. Creating parts additively allows designers to create new geometries impossible to create by conventional, subtractive manufacturing means. Advances in technology have also allowed designers to rapidly prototype their part, sometimes even in the final build material, to check fit, function, and get a better feel for the practical use of the part. AM is of interest to a multitude of manufacturing industries but is of special use to the medical, aerospace, defense, and automotive industries. Additive processes allow biomedical designers to quickly and relatively cheaply fabricate medical implants and prostheses custom tailored to the individual patient. This increases the effectiveness of the implant or prosthetic fabrication process and means shorter recovery times and better performance of the implant. A major use for additive processes in aerospace and automotive industries is manufacturing low density parts. In aerospace and automotive racing applications overall vehicle weight must be minimized to

optimize performance. If full density parts are not structurally necessary within the design of a part, weight and material cost can be saved by manufacturing a partially hollow, or porous, part using AM. Weight can also be of concern in defense applications but another major area of interest is the use of additive processes aboard navy and coast guard vessels. If a part breaks shipboard during a sea tour, the part must either be replaced at the end of the tour when the ship returns to port or another vehicle must deliver a replacement part to the ship. This is cost intensive in both time and energy. AM allows for replacement parts to be manufactured in real time as needed saving time, transportation costs, and ensuring full mission capability throughout the ship's tour of duty.

1.1.1 Early Processes

The field of AM has existed in some form since the mid-19th century [1]. The technology finds is roots in the fields of topography and photosculpture. In early topography, scientists worked to create 3D representations of topographic maps common at the time to show changes in elevation. In photosculpture a series of cameras are used to take pictures of an object from a variety of orientations and the series of photographs are used by a sculptor as filters in photoresist processes to build a 3D model representing the physical object. These processes show little commonality with the processes we associate with AM today, but share the important element of 3D objects being built in a layer-by-layer fashion.

1.1.2 Stereolithography

The first modern AM technique to come to fruition was a stereolithography process developed by 3D Systems in 1986 [2], [3]. In the stereolithography process, a light source is focused on a pool of photo-polymeric liquid to create layers of material. This means that when light interacts with the liquid, it solidifies through a polymerization process. The location the

light source interacts with the pool is controlled by a computer aided design (CAD) model supplied by the user. This CAD model is then segmented into many layers and saved in the form of a Stereolithography, or Standard Tessellation Language, (STL) file. Each layer is built by subjecting the photosensitive pool to the light source in accordance with the STL file. After building each layer, the build platform supporting the solidified polymer drops one layer thickness lower into the liquid pool and the next layer is built by the light source. This process is repeated until the entire part has been built [3]–[5].

1.1.3 Fused Deposition Modeling and Inkjet Printing

Other early processes typically seen used with plastic build materials are Fused Deposition Modeling (FDM) and Ink Jet Printing (IJP) [2]. In FDM, a continuous strand of material is forced through a nozzle to place the material in the proper locations dictated by the CAD model. The molten fibers of materials are laid down in a crisscrossed fashion between layers to reduce anisotropic effects associated with the process [6]. FDM is mainly used for plastics but can also be used to build ceramic and metallic parts by depositing binder material into a powder bed instead of depositing structural material onto a build plate.

IJP follows a similar principle, however, instead of jetting a continuous stream of material, small droplets of binder material are deposited on the top surface of a powder bed and, when solidified, bind together the individual powder particles in the bed to form a cohesive layer [7]. The process can also be utilized in such a way that the jetted material is structural in nature rather than a binder material. In this utilization, the flow characteristics and self-wetting characteristics of the material are of utmost importance. IJP is used for polymers, wax materials, and can be used for ceramics and finds special use in microelectronics and micromechanical system fabrication [8].

In both FDM and IJP, like stereolithography, the final part is built up layer-by-layer in accordance with the CAD model. As the use of additive methods increased in polymeric construction, increased interest developed in creating metallic and ceramic parts additively. In addition to adapting the FDM to use in metals and ceramics by using binder materials other processes were proposed that did not require use of binder materials.

1.1.4 Laser Engineered Net Shaping

One of the first of these newly proposed methods was Laser Engineered Net Shaping (LENS) [9]. In the LENS process metallic powders are jetted from above the build surface impingent upon a laser beam which heats and melts the powders onto the build surface. The laser and the powder jet are controlled by the CAD model to move the melt pool to the proper location within the build volume.

1.1.5 Laminated Object Manufacturing

Another technique, Laminated Object Manufacturing (LOM), makes use of both additive and subtractive methods. In this technology thin sheets of material are cut into the proper shape, as governed by the CAD model, and the sheets are bound together under pressure and heating to create 3D laminated part.

1.2 Powder Bed Processes

1.2.1 Binder Processes

The next major step in the AM community came in the development of the powder bed process. In this process, a layer of metallic, polymeric, or ceramic powder is raked across the build plate to create a thin layer of material. A heating source beam is then used to selectively fuse the powder in the proper locations governed by the CAD model, creating a layer of solid material. After each layer of solid material is built, the build plate drops down one layer

thickness and a new layer of powder is raked on top of the previously built layers. This layer is then fused conformant to the CAD model and the process continues until the final part has been completely built [10].

The work presented by the author focuses on the use of power bed processes to produce metallic parts additively. Within the metallic powder bed AM processes two major subcategories exist – melting/sintering processes and material binder processes.

In the binder processes two materials exist within the powder bed, a structural material and a binder material with a lower melting temperature [11]. The source beam acts to melt the binder material and capillary forces draw the molten binder between the structural powder particles. As the binder solidifies it holds the structural particles together to create a cohesive layer. At this point the part may be in its final form, or a variety of post-processing procedures may be required. If the bound part is held at elevated temperature for sufficiently long time, the structural particles will sinter together through a mass diffusive process and the binder material may be removed without losing part structure. Issues with the binder processes include increased porosity and decreased strength in the final part [2], [11], [12]. Because of the lack of structural continuity in binder processes, melting and sintering processes demand a greater focus in the literature. In the melting and sintering processes, the source beam acts to heat and consolidate the structural metallic powders into a cohesive layer through various consolidation phenomena.

1.2.2 Consolidation Phenomena

Kruth et al. [11], [12] presents an overview of the various consolidation phenomena present within powder bed processes. Solid state sintering is a process in which particles are combined by inter-particle mass diffusion. This requires a lower heating value and processing

temperature than the other consolidation phenomena but a longer application time due to the relative long time scale of mass diffusion in solid materials. The particles do not melt, but fuse together forming small necks between each particle. This process is the slowest occurring consolidation phenomena considered and leads to parts with the highest porosity.

Liquid state sintering typically occurs in powder beds consisting of multiple powder materials, the binder processes. One set of materials act as a binder while the other materials act as the structural material of the part. The binder melts under heat application and is forced into the voids of the structural powder by intense capillary action. The part is known as a "green part" when in the state it leaves the initial binding process. The mechanical properties of the final part are controlled by the structural material and the binder can either be left in the part or removed to vary the porosity of the final part. Post processing and heat treatment may be utilized on the green part to allow for solid state sintering within the structural material to create a more structurally sound final part.

Partial melting processes typically occur in single material or alloy powder beds and may contain melting temperature reducing compounds. In this process, the smaller particles in the bed melt more quickly than the larger particles and are forced into voids between the larger particles by capillary action. This creates a more uniform, denser part than in liquid state sintering. The part is still not fully dense under this consolidation phenomenon. The part therefore retains the thermophysical and mechanical properties of the powder instead of the solid material.

In full melting processes, the heated area is melted entirely and solidifies to form a fully dense part. This means that the final part has all of the characteristics and properties of the solid material and typically performs better than parts of higher porosity.

1.2.3 Melting and Sintering Processes

Because of the porosity and structural integrity issues associated with binder processes sintering and melting processes are more widely used in the aerospace and defense industries as well as the biomedical industry, depending on application. Within the group of melting and sintering processes there are two subcategories; laser based and electron beam based. The most obvious difference between these groups of processes is the heating source being used. In the laser process, a variety of laser beams can be used to melt the powder and choice of laser is dependent on the material being used and the application of the final part. In the electron beam melting processes, an electron gun is used as the heating source.

The first successful powder bed sintering process was Selective Laser Sintering (SLS) introduced in 1987 at the University of Texas for use with plastic materials [13]. In SLS, when using metallic powders, the laser heat source is not powerful enough to sinter metal powder by itself so the metal must first be coated with a polymer binder. As the laser scans the powder bed, the binder material is melted while the metal powder core remains unmelted. Capillarity forces the molten binder in-between the solid metal particles and as the binder solidifies, the powder is bound into a porous part. As laser technology advanced and power input increased, the SLS process could be utilized by melting the smaller particles within the powder bed. At the time, the laser still did not have the requisite power to produce enough heat to fully melt the larger particles. Like the binder materials, the molten material from the small particles is forced into the voids between the large particles by capillarity. This is an example of the partial melt consolidation mode.

As technology further advanced and lasers became capable of providing energy sufficient to fully melt the entire range of powder particle sizes, the method of Selective Laser Melting

(SLM) was introduced. SLM was developed by increasing the laser power and decreasing the scan speed in SLS processes. The increased power and decreased scan speed allowed metal particles to be melted and solidify into a single part but can cause less desirable properties in the formed part [4]. Due to the finished part advantages of SLS, and the desire to remove binding elements from the powder bed, EOS developed direct metal laser sintering (DMLS) in 1995 [14]. In DMLS, the laser is able to partially melt or sinter the metal particles in the powder bed so no binder material is required. The partially molten particles act as the binder material in the build volume and create gates between solid particles [6].

Responding to the desire to build fully dense parts and decrease build times, Arcam developed electron beam melting (EBM) in 1997 [4]. EBM is able to achieve much higher scan speeds due to its stationary electron beam heat source being deflected by electromagnetic fields. Since the process fully melts the powder, full density parts can be created using EBM. The EBM process also allows for faster build times through use of Arcam's Multibeam® technology. In the Multibeam process, the electron beam is diverted across many locations within the build plane while outlining the shapes to be built within that layer of the part. This gives the appearance of the beam acting on multiple locations within the build plane simultaneously. This also allows for more than one melt pool to be active within the layer at any given time, reducing the build time required to outline each layer and, therefore, reducing the total build time required for the part. The hatch scanning, or filling in of the outlines, requires more finesse to ensure proper part properties and interlayer adhesion. Therefore, it must be completed by producing a single melt pool at any given time and the beam must operate at slower scan speeds to more deliberately maintain a consistent melt pool.

Figure 1 shows schematics for DMLS and EBM. Since both processes are powder bed processes, most of the operating characteristics are similar between the two manufacturing techniques. Some differences include a single sided powder hopper in the DMLS system while the EBM system feeds powder from both sides of the build volume. In DMLS, the laser optical system moves in the xy plane to allow the beam to act perpendicularly to the powder bed. In EBM, the electron gun is stationary and the beam is deformed by a series of electro-magnetic lenses to change the location the electrons interact with the powder bed.

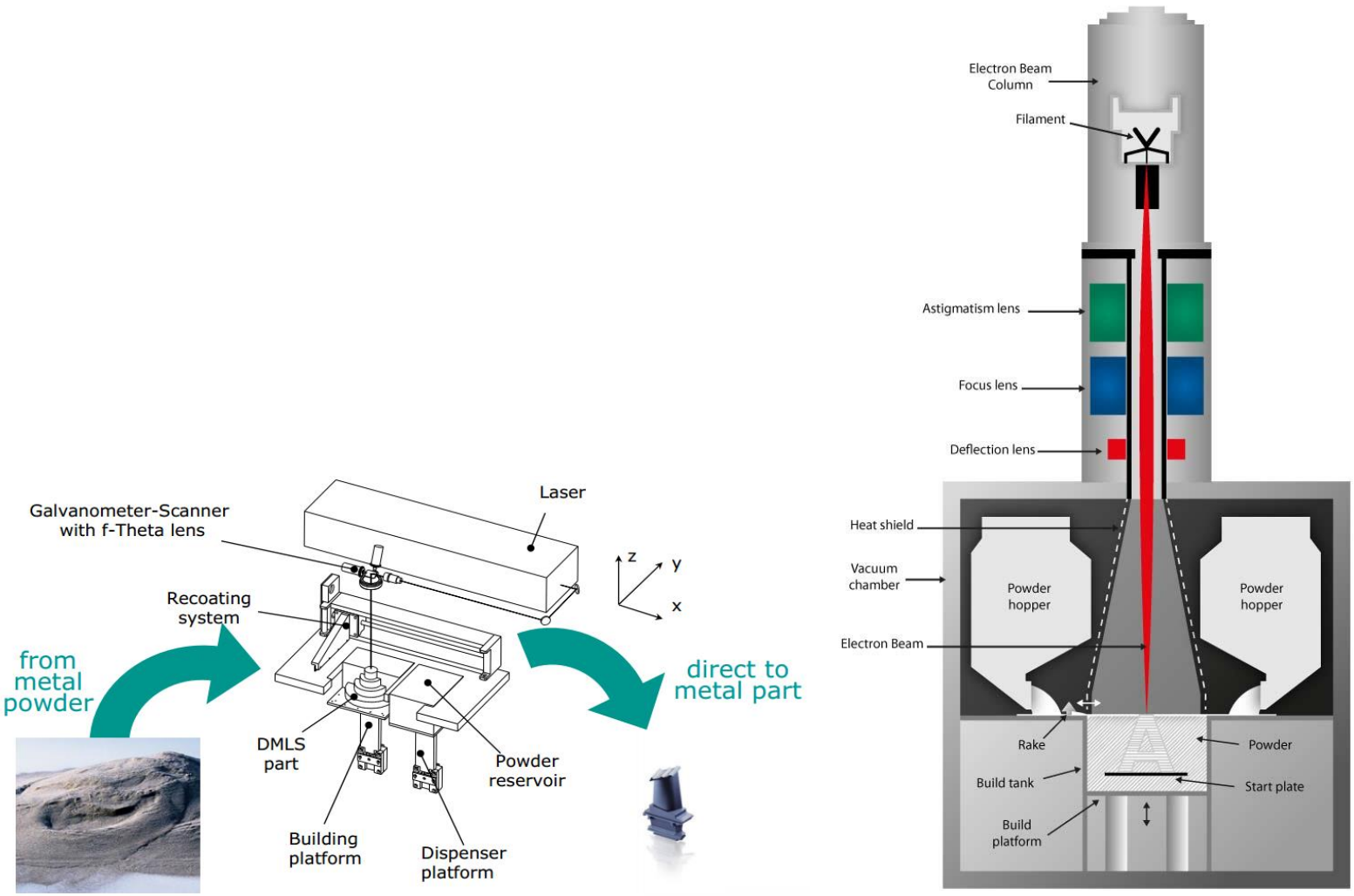

Figure 1: DMLS[15] and EBM[16] schematics

1.3 Process Parameters

It is of utmost importance to consider the various process parameters that go into the SLS/SLM and EBM processes. Each process parameter has the potential to affect the quality of the final part and the characteristics of the build. In order to ensure a desirable part is built, the proper set of process parameters must be used and varies depending on part material and requisite part properties. Many studies exist in the literature discussing what process parameters may be varied in the powder bed process and what effect changes in the parameters have on final part quality. Table 1 summarizes some recent studies investigating the main process parameters and their effect on overall part quality.

Parameter	Effects on Part
Preheat Temperature	Higher preheat temperatures lead to less dramatic cooling and part favors equiaxed grain microstructures [17].
Beam Diameter	Beam intensity is spread over a larger area resulting in slower cooling rates, lower maximum temperatures and less beam penetration [18].
Scan Speed	As scan speed decreases, the time the beam emits heat to each particle increases, increasing melting and leading to decreased porosity and increased part density. Slower scan speeds also decrease the microhardness of the part [19].
Layer Thickness	Increased layer thickness decreases the overall build time and decreases the dimensional precision of each layer.
Powder Particle Size and Distribution	Smaller particles and denser packing results in heat being better transferred through the powder into lower levels. This means lower temperatures and quicker cooling. This also means denser built parts in sintering and it also means shallower melt pools in melting [18].
Beam Power	Powder is subjected to higher heat and melts more thoroughly. Beam penetrates deeper into the build volume [18].

Table 1: Effects of varying process parameters

Various modeling studies have also been conducted to determine the effects of changing process parameters on final part quality. Roberts et al. [20] considered residual stress formation due to thermal cycling and characteristic time scales for conduction and recoating in the SLM process. Simchi [21] performed experiments in a variety of ferrous materials built by DMLS to assess the effect of process parameters on part density. The study concluded that, all other parameters held constant, increasing beam power and decreasing scan speed both increase part density. It was also suggested that high beam power increases the likelihood of delamination of sintered layers and formation of large cracks in the built part. Vayre [22] formed a study to consider two aspects of the AM process, in EBM particularly, that are typically disregarded: powder removal and support structure design. Powder removal was found to be dependent on built part features and powder removal application time. To assess the influence of part features on the powder removal process, a series of hollow tubes varying from 4 mm to 14 mm in diameter were fabricated. The depth of the tube in which powder was successfully removed was then measured. Powder removal depth increased as tube inner diameter increased. Therefore the larger the space between part features, the more efficiently unused powder is removed from the build. It was additionally determined that removed powder volume also increases with increased application time.

1.4 Gaps in Literature

There is still room for much research into modeling and simulating thermal transport phenomena in metallic powder bed AM processes. Current models existing in the literature typically do not have proper breadth to consider both laser and electron beam heating – they consider only one or the other. Current studies also only consider the effects of limited process parameters. Additionally, current models in the literature only focus on describing the process in

building one material. At this stage in the process lifecycle more efforts are needed in applying the powder bed AM processes to a broad base of novel engineering materials. By understanding how process parameter changes affect build quality in many materials, powder bed processes can be best optimized for each material type of interest.

1.5 Objectives

The objective of this work is to move beyond existing literature by predicting required process parameters for materials that have not been successfully fabricated using powder bed processes. A broad base of novel engineering materials is considered within this thesis to include titanium alloys, stainless steel, aluminum alloys, and nickel superalloys. Observed trends between material selection and process parameter selection are presented as well as comparisons of all materials built with similar process parameter sets. It is critical to provide process engineers with an initial estimate of the parameters that could be used safely in production of these materials. With a greater understanding of how thermal transport changes from material to material; process parameters can best be adapted to each material and selected intelligently to avoid trial and errors and safety issues. This will make powder bed processes a more powerful manufacturing tool and give more freedom to designers when selecting materials and process parameters.

CHAPTER 2 Modeling Setup

A variety of studies are presented in the literature that describe thermal transport phenomena present in metallic powder bed processes [18], [20], [23]–[26]. These models require a certain level of complexity in order to fully describe the physical phenomena present within the powder bed AM process. It can, for example, be necessary to model the process

transiently and consider moving heat sources, phase change, and various mass and heat transfer phenomena simultaneously. Additionally, both micro- and macro-scale transport phenomena need to be considered to fully describe the physics of the powder bed processes. Figure 2 below outlines the thermal transport phenomena present within the processes. At the macroscopic scale convective, conductive and radiative transport are considered between the solidified regions of the build volume, the build plate, and the build atmosphere. The same transport mechanisms exist between individual powder particles however the size scale of these transport mechanisms adds complexity to the physical description of the transport. Fluid motion can also exist within the melt pool resulting from thermal driven surface tension gradients.

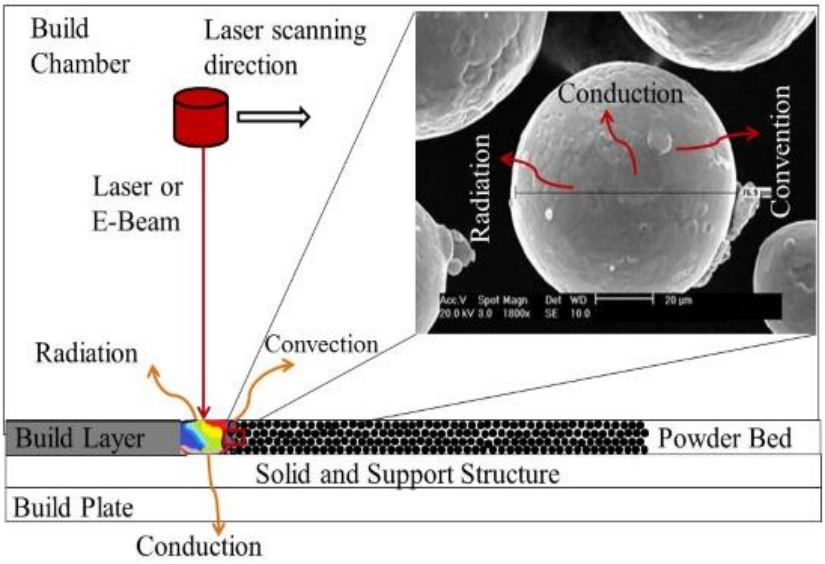

Figure 2: Multiscale thermal transport phenomena

2.1 Literature Review

Roberts et al. [20] created a model describing the heat flow in laser processes, particularly in Ti6Al4V. In the Roberts model, the laser was modeled as a moving heat source with a heat generation function consisting of a Gaussian distributed, radially decaying, intensity in the build plane and linearly decaying intensity along the depth into the part. In addition, the Roberts model incorporates element birth and death to allow for the "creation" of new layers of

powder throughout the transient analysis, modeling multiple layers of the laser melting process. Using this technique, it was shown that heat dissipation throughout the part occurs at a much faster time scale than recoating, or the addition of new layers of powder, occurs. Residual stress concerns in the final part arise because of rapid thermal cycling as the part is subjected to elevated temperatures and fast heating and cooling with the addition and building of each layer in the part. Roberts assumed that convective and radiation terms could be neglected in the model because the bulk of heat transfer is done by conduction through the powder and solidified titanium into the build plate. Roberts' simulations suggest that layers applied later reach higher maximum temperatures because the conductivity of the build material, titanium, is less than the conductivity of the heat sink or base plate material, stainless steel, meaning heat cannot flow through the part as quickly. As the simulation progressed layer-wise, Roberts also observed the steady state temperature increased slightly, but consistently, after the addition of each layer.

Shen and Chou [18] created a model to simulate the EBM process, also in Ti6Al4V. Similarly, the Shen and Chou model also uses a moving source heat generation with a Gaussian radial distribution and linear depth decay to model their beam. This model aimed to investigate how thermal gradients and heating/cooling rates change when a variety of build parameters are adjusted, such as powder bed porosity, powder versus solid substrates, and electron beam effective diameter.

Previous studies have concluded that thermal conductivity [20], [23] and emissivity [27] vary greatly between solid and powder and therefore cause different thermal resistances between solid layers of material and powder layers. These properties are not constant for a given material across all powder bed manufacturing processes. They, rather, are dependent on such process parameters as the porosity percentage of the powder bed and the heating source type. As may be

expected, the materials used in the powder bed process react differently when subjected to heating from lasers; an optical transfer phenomenon, and electron beams; a kinetic transfer phenomenon.

Kolossov [23] and Sih [27] show respectively that as porosity increases, the effective conductivity of the powder bed decreases and the emissivity of the powder bed increases. Conductivity studies [20], [23] were conducted assuming an inert gas build atmosphere, characteristic of the SLM and SLS processes, which allows convective cooling of the top surface of the powder bed. This assumption does not hold for the EBM process since EBM is designed to operate in a high vacuum.

Considering the effect of vacuum on the process, Shen and Chou [18] determined that as porosity in the powder bed decreases, so does the maximum temperature and size of the melt pool. Shen and Chou postulate that this is due to lower thermal resistances seen in the solid material than in the powder. This relationship is the result of voids existing between individual particles that have much lower thermal conductivities that the solid materials and therefore cannot transfer heat effectively. As porosity increases, the conductive potential of the powder bed is lessened and maximum temperature and thermal gradients within the melt pool are increased. By decreasing the effective beam diameter, while keeping beam power consistent, the beam intensity decreases. As expected, this causes a decrease in the simulation maximum temperature, decrease in thermal gradient strength, and shrinking of melt pool geometries. When powdered materials are considered as the build substrate opposed to solid material, such as when building overhanging part features, melt depth is increased. This is because thermal conductivity of powdered materials are less than the corresponding solid materials and heat cannot as efficiently dissipate depth wise into the build volume.

Dong et al. [24] also created a transient finite element method (FEM) model using a Gaussian distributed moving heat source. Dong discusses paradigms to numerically determine material properties such as density, conductivity, etc. during each step of the solution. Since the model presented in this thesis is performed in ANSYS Mechanical APDL, a program which automatically interpolates the material properties at each step in a transient analysis, the approaches discussed in Dong do not have a direct impact on the author's modeling efforts. The model presented by Dong allows for convective and radiative cooling at the top surface of the powder layer and assumed an adiabatic condition at the bottom of the powder layer. The adiabatic boundary condition at the bottom of the powder bed does not apply in a complete description of powder bed processes since heat transfer into the build plate is essential in accurately modeling the process. The model presented in this thesis instead adds volumes representing solidified layers and the build plate then an adiabatic boundary condition is applied to the bottom of the build plate.

2.2 Global Governing Equations

2.2.1 Continuity and Momentum Balance

Due to the short time scale of the performed analysis, on the order of 10's of ms total simulation time, fluid motion is assumed negligible. Through application of this assumption, mass conservation is automatically satisfied across the entire computational domain at every time step. Additionally, it is assumed that only thermal loading exists within the model and the geometry is allowed to freely expand and contract under such thermal loading. For this reason a momentum balance does not provide any meaningful information to the computational domain.

2.2.2 Energy Balance

The true analysis is performed by evaluating the energy balance at every node within the computational domain at each time step. The developed model considers phase change by gradually adding energy from latent heat of fusion into the temperature dependent specific enthalpy definition through the mushy zone region between solidus and liquidus temperatures. Since fluid motion is assumed negligible, specific enthalpy is synonymous with specific internal energy and the author's latent heat addition is consistent with first principles of phase change phenomena.

To reconcile thermophysical property differences between the powder, molten, and bulk solid materials, separate material modes are created within ANSYS for each material type. The addition of a "resolidified" material model allows for a time history of elements that were solidified from the molten state at some point before the end of the simulation. This resolidified model has the same properties as the solid model; it merely acts as a way to differentiate those elements that were melted at some point during the simulation against those that remained solid through the entire duration of the simulation. During each time step, after the convergence criteria have been satisfied, all nodes within the domain are queried to find elements where all included nodes are above the liquidus temperature. If these elements are currently assigned the material id for powder material, they are updated with properties from the liquid model. At the same time, all elements with all contained nodes below the solidus element are found. If these elements are assigned the material id for liquid material they are updated with the properties for the resolidified material.

From Faghri [28], equation 1 below depicts the full energy differential equation for a single component system that governs energy balance within each finite element.

$$\rho \frac{D}{Dt}\left(e + \frac{\boldsymbol{v}\cdot\boldsymbol{v}}{2}\right) = -\nabla \cdot \boldsymbol{q}'' + q''' + \nabla \cdot (\boldsymbol{\tau} \cdot \boldsymbol{v}) + \sum(\rho \boldsymbol{X}) \cdot \boldsymbol{v} \qquad \textit{Eq. 1}$$

The energy balance differential equation uses the following parameters; ρ: density, e: specific internal energy, $\boldsymbol{v}$: velocity vector, q'': heat flux vector, q''': heat generation, $\boldsymbol{\tau}$: deviatoric stress tensor, and X: specific body force acting on the element. Also note that $\frac{D}{Dt}$ represents a material derivative and can be expanded as seen in equation 2 where ψ is some parameter being differentiated.

$$\frac{D\psi}{Dt} = \frac{\partial \psi}{\partial t} + v \cdot \nabla \psi \qquad \textit{Eq. 2}$$

X can be any body force resulting from conservative potential fields acting on the finite element. The small size scale of the model means that gravity effects may be neglected. Additionally magnetic effects are considered negligible therefore the body force term can also be neglected. By additionally applying the "no motion assumption" within the domain, the kinetic energy term within the material derivative and the stress term both become negligible. The convective term within the material derivative also goes to zero under this assumption, leaving only time differentiation from the material derivative. By applying the relationship between energy, temperature and specific heat outlined in equation 3, the familiar Heat Equation is derived as seen in equation 4.

$$de = cdT \qquad \textit{Eq. 3}$$

$$\rho c \frac{\partial T}{\partial t} = -\nabla \cdot \boldsymbol{q}'' + q''' \qquad \textit{Eq. 4}$$

In these two equations, c represents the specific heat and T represents the temperature of the finite element. Equation 5 below shows the constitutive model for the heat flux in the system assuming Fourier's Law applies for conduction within the domain. Equation 6 is added into the

heat flux term at the top surface where radiative cooling is allowed to occur. Equation 7 describes the heat generation within the domain resulting from the laser or electron beam interacting with the domain and is based on the work originally of Rouquette [26], and later seen in Shen and Chou [18], Roberts [20], and Dong [24].

$$q'' = -k\nabla T \qquad \text{Eq. 5}$$

$$q'' = \varepsilon\sigma T^4 \qquad \textit{Eq. 6}$$

$$q'''(x,y,z) = f(z)\frac{8\alpha\dot{W}}{\pi\Phi^2}e^{\frac{-8[(x-x_c)^2+(y-y_c)^2]}{\Phi^2}} \qquad \textit{Eq. 7}$$

With $$f(z) = \frac{2}{\delta}\left(1-\frac{z}{\delta}\right)$$

In equation 5, k represents the thermal conductivity. In equation 6, ε represents the emissivity of the material and σ is the Stefan-Boltzmann constant. Equation 7 makes use of the following parameters; α: thermal absorptivity, $\dot{W}$: beam power, Φ: effective beam diameter, and δ: beam penetration depth. x_c and y_c describe the center of the beam. Thermal absorptivity is a material property, while beam power, effective beam diameter and penetration depth are user defined parameters for this model.

Figure 3 graphically depicts the heat generation function. The top of the conical feature shows how heat is generated in each xy planar slice of the conical distribution. The center of the planar slice is red to represent the highest beam intensity existing at that point. The beam intensity diminishes radially outward until it reaches the effective radius of the beam which is defined as the radial distance at which energy density is reduced to $1/e^2$ [29]. The intensity, along with the effective radius of the beam, decreases with depth into the build volume. Each xy plane within the cone has a similar heat distribution to the top plane, with the caveat that the maximum

plane beam intensity decreases with depth into the build volume. In figure 3, the intensity contours are normalized by the maximum beam intensity.

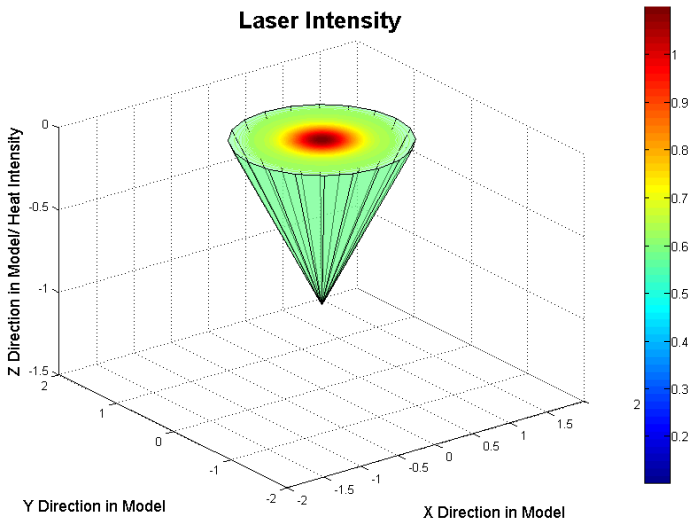

Figure 3: Beam intensity

2.3 Model Geometry

ANSYS Mechanical APDL was used to perform the transient FEM analyses including melting and solidification presented in this thesis. Since previous studies have concluded that convective cooling is an insignificant transport mode [20] within the powder bed compared to conduction, only the build volume needs to be considered in this analysis. The build volume is modeled as a rectangular block consisting of a top layer of powder material, followed by a layer of solid material, and an AISI 4130 steel build plate. This solid layer is representative of powder layers that have already been built and the model therefore considers a part in the middle of its build. Thermal history of the powder bed, however, is not considered in this model. Figure 4 shows the coordinate system set up for the model, along with the beam line of action. The dimensions of each of these layers are shown in table 2. To allow for consistent comparison

between laser and EBM processes, a constant powder layer thickness was assumed across both processes.

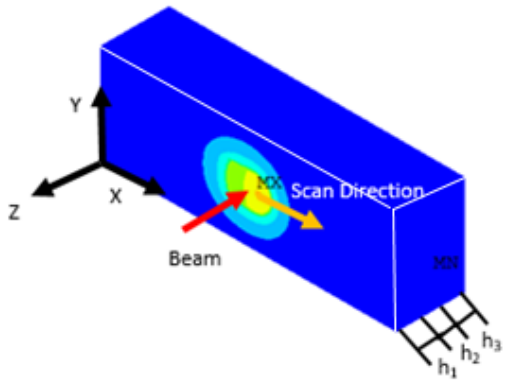

Figure 4: Block orientation, beam direction and direction of motion. h_1, h_2 and h_3 denote the thickness of powder, solid and build plate layers.

Dimension	mm
Model X Dimension	9
Model Y Dimension	3
Powder Layer Thickness (h_1)	0.04
Solid Layer Thickness (h_2)	0.9
Build Plate Thickness (h_3)	1

Table 2: Model dimensions

The model considers radiation at the top surface of the powder layer to the build atmosphere. Convective cooling at the top of the powder layer and convective effects within the build volume are neglected because the majority of heat is transferred by conduction from the powder into the solid and the build plate layers [20]. The sides of the block are held constant at the initial temperature and the beam starts and ends 3 mm from the left and right sides of the block respectively to simulate scanning within a larger powder bed.

CHAPTER 3 Material Properties

The specified chemical compositions for the materials studied within the confines of this thesis can be found in appendix A. The chemical composition of the materials is of interest since it dictates, in part, the microstructural development within each material upon solidification as previously explained. Microstructural development plays an essential role in determining the mechanical and thermophysical properties of the bulk material. In developing a thermal model for powder bed AM techniques, thermophysical properties of the material are of utmost importance.

The thermophysical properties considered include thermal conductivity, density, specific heat, specific enthalpy, and radiative properties (thermal absorptivity and emissivity). These properties are input into ANSYS as functions of temperature and are used to solve the system of governing energy equations at each node in the computational domain. These properties are also a function of material state where powder materials and bulk solid materials have different effective properties due to voids existing in the power bed that are assumed to not be present within the solidified material. Liquid properties can also vary from the solid properties both because of elevated temperatures and different atomic phenomena present within liquids that are less important in solids.

3.1 Effective Thermal Conductivities

3.1.1 Powder Conductivity Theory

For powdered materials an effective thermal conductivity is introduced that takes into account conduction, convection, and radiation transport phenomena between individual powder particles. By adopting an effective conductivity approach a macro-scale thermal analysis can be used to consider both transport between particles in the powder bed and transport out of the

powder bed into the solid and base plate layers. This means a single scale modeling paradigm can be used, reducing the computational resources and time needed to solve the problem. Two effective powder conductivity correlations have been utilized in the author's work; the Hadley [30] correlation, labeled equation 8, is used for unsintered powder beds – such as those seen in SLM processes, while the Agapiou [31] correlation, labeled equation 9, is used for initially sintered powder beds – like those seen in EBM.

$$\frac{k_e}{k_g} = (1-a)\frac{\eta f_0 + \frac{k_s}{k_g}(1-\varepsilon f_0)}{1-\eta(1-f_0)+\frac{k_s}{k_p}\eta(1-f_0)} + a\frac{2\left(\frac{k_s}{k_g}\right)^2(1-\eta)+(1+2\eta)\frac{k_s}{k_g}}{(2+\eta)\frac{k_s}{k_g}+1-\eta} \qquad \textit{Eq. 8}$$

Where:

$$f_0 = 0.8 + 0.1\eta$$

and

$$\log(a) = \begin{cases} -4.898\eta & 0 \le \eta \le 0.0827 \\ -0.405 - 3.154(\eta - 0.0827) & 0.0827 \le \eta \le 0.298 \\ -1.084 - 6.778(\eta - 0.298) & 0.298 \le \eta \le 0.580 \end{cases}$$

$$\frac{k_e}{k_s} = \frac{1-A_1\eta}{1+A_2\eta+A_3\eta^2} \qquad \textit{Eq. 9}$$

Where:

$A_1 = 2.05 \qquad A_2 = 0.68 \qquad A_3 = -4.20$

Equations 8 and 9 make use of the following parameters: k_e: Effective powder thermal conductivity; k_g: Void (build atmosphere) fluid thermal conductivity; k_s: Bulk solid thermal conductivity; a: Scaling function of powder bed porosity; η: Powder bed porosity; f_0: A second scaling function of powder bed porosity; A_1, A_2, A_3: Scaling constants. The scaling factors A_1, A_2, A_3 are taken from Agapiou and represent the best fitting model compared with experiments in

steel powders. The scaling factors are a function of packing orientation and I assume that the same model can be used across the materials considered in this work.

When sintering occurs within the powder bed, the contact patch between two adjacent powder particles widens and, as can be expected, the conductivity between powder particles increases. For this reason, the Agapiou correlation yields higher effective conductivities for the same materials than the Hadley correlation.

3.1.2 Liquid Conductivity Theory

Since the liquid properties within the literature typically refer to a quiescent fluid additional transport considerations must be made when fluid motion is present. It is known that due to metallic bonding molten metals have very high surface tensions. Since surface tension is a function of temperature, large thermal gradients, such as those seen within the melt pool in powder bed processes, develop large surface tension gradients within the fluid. A large enough surface tension gradient acts as a driving potential for fluid flow. This phenomenon is commonly known as the Marangoni or thermocapillary effect, and the cooling phenomenon resulting from this fluid motion is known as thermocapillary convection or Bénard-Marangoni convection.

Since density is also dependent on temperature large thermal gradients develop density gradients within a fluid leading to buoyancy effects. Buoyancy is the mass transport phenomenon that occurs when fluids of different densities are driven to different depths under interaction with a gravity field. In this case, the gravity field is earth's gravity field. Lighter fluids are forced to float above heavier fluids so it is expected that thermal gradients must be, at least in part, in a vertical direction in order for buoyancy to be considered. In the powder bed process, thermal gradients are much stronger in the radial direction than in the vertical direction,

as evident from thermal contours seen in the results section. Beyond this, the hottest fluid elements are at the highest point in the melt pool to begin with since the fluid is heated from above the melt pool, not below. These two factors, along with the small size scale, 100's of μm in the radial direction and 10's of μm in depth, and small time scale, 1's of ms, it is expected that buoyancy is not a dominant transport mode.

A modified Bond number (Bo) is used in scale analysis of the energy balance within the melt pool to determine the relative effects of thermocapillary and buoyancy. The dimensionless Bo is derived by dividing the scaled gravity force by the scaled surface tension force. The gravity force, in this case, results from the temperature dependent nature of density existing in a gravitational field since large thermal gradients exist within the melt pool. The surface tension force results from the temperature dependent nature of surface tension and the large thermal gradients in the melt pool. A high Bo (>>1) means that buoyant forces are dominant over surface tension forces and surface tension driven flow can be neglected. A low Bo (<<1) means the opposite is true and gravity driven flow can be neglected.

Another dimensionless group, the Marangoni number (Ma), is calculated to determine the relative effects of viscous forces within the melt pool and surface tension forces. Ma is derived by dividing the scaled surface tension force by the scaled viscous force. A high Ma means that surface tension forces are dominant and a low Ma means that viscous forces are dominant. Table 3 shows the definitions of these two dimensionless quantities and their values for each of the materials considered in this thesis, each with a beam power of 150W. Ti6Al4V was chosen to represent titanium alloys, stainless steel (SS) 316L to represent steels, Al 7075 to represent high strength aluminum alloys, and Inconel (IN) 718 to represent nickel superalloys. For simplicity the Bo values presented in this table are listed in scientific notation.

Material	Marangoni Number $Ma = -\frac{d\gamma}{dT}\frac{L\Delta Tc}{\nu k}$	Bond Number $Bo = \frac{\frac{\partial \rho}{\partial T} g L^2}{\frac{\partial \gamma}{\partial T}}$
SLM Ti6Al4V	1.08E4	7.94E-7
EBM Ti6Al4V	2.99E4	
SLM SS316	8.745E3	1.70E-6
EBM SS316	2.48E4	
SLM Al7075	3.49E2	1.83E-7
EBM Al7075	3.42E3	
SLM IN718	4.301E3	2.23E-5
EBM IN718	1.17E3	

Table 3: Marangoni and Bond Numbers

In table 3 the following symbol definitions, not previously defined, are used; γ: surface tension; *v*: kinematic viscosity; *L*: characteristic length; g: acceleration of gravity; *ΔT*: change in temperature between theoretical maximum temperature and solidus temperature. In the case of both Ma and Bo the characteristic length is considered to be an assumed melt pool radius determined through user experience, comparison against experimental findings, or previously simulated results.

A Ma is calculated for each material in both EBM and SLM processes due to the fact that the change in temperature, ΔT, in the Ma definition is process dependent as well as material dependent. Bo, however, is only dependent on material properties and is independent of the build process being used. For this reason a single Bo for each material fully characterizes the comparison between buoyancy and thermocapillary in that material. For each material considered, Bo is much smaller than one, regardless of assumed melt pool radius since any realistic melt pool radius is also much smaller than one, so gravity effects within the melt pool can indeed be neglected. Additionally, Ma is very large for all materials and all processes so viscous effects can also be neglected generally in the melt pool model. Therefore, the only significant factor affecting fluid motion is the thermocapillary effect.

To keep the analysis simple, and as an alternative to coupling a computational fluid dynamics (CFD) analysis to the FEM model, an effective liquid conductivity is derived that encompasses the advective effects from fluid motion within the melt pool. In order to perform such an analysis, a convective heat transfer coefficient representative of the fluid motion is required. Rigorous calculation of an effective liquid conductivity requires iteratively finding melt pool radius from simulation and updating the conductivity if experimental geometry is not available. This thesis lays out the procedure for determining effective conductivity for liquid materials and does not perform this iterative analysis. In the case of Inconel, experimental melt pool radii are used. In the other materials previous numerical studies are used to determine a baseline melt pool radius.

Straub [32] presents a correlation between Ma and Nusselt number (Nu), defined below, for very high Ma flows. Straub conducted his analysis in a microgravity environment since under normal, macro-scale, conditions buoyant effects are much more significant than surface tension effects. Since it has already been shown that thermocapillary effects are the dominant transport phenomenon, it is assumed the microgravity findings apply at the small size and time scales of the developed model. By taking data points from the work by Straub, figure 5 recreates the Ma-Nu relationship proposed. By interpolating from this data, using the logarithmic fit equation labeled equation 10, a Nu for each material can be determined.

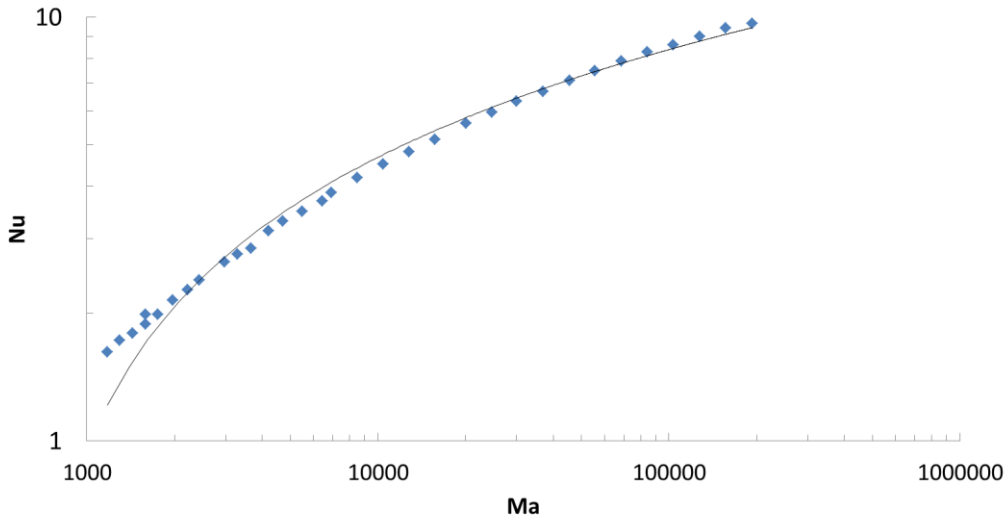

Figure 5: Straub's Nu-Ma Relationship [32]

$$Nu = 1.6129\ln(Ma) - 10.183 \qquad \textit{Eq. 10}$$

$$Nu = \frac{hL}{k}$$

After determining Nu for each material the heat transfer coefficient, *h*, can be calculated from the Nu definition. With the heat transfer coefficient determined a heat flux balance is considered as seen in equations 11 and 12. On one side of this balance is the actual conductive and convective heat fluxes expected within the system. The conductive transport follows Fourier's Law and the convective transport follows Newton's Law of Cooling. On the opposite side of the balance is an effective conductive transport, represented by k_{eff}, that will be used within the FEM model.

$$q''_{cond} + q''_{conv} = q''_{cond,eff} \qquad \textit{Eq. 11}$$

$$k_{liq}\nabla T + h\Delta T = k_{eff}\nabla T \qquad \textit{Eq. 12}$$

In the two conduction flux terms the thermal gradient, ∇T, can be approximated as change in temperature over some characteristic length. In this case, the characteristic length is the melt pool radius and the temperature change is the same ΔT introduced in the Ma definition.

The temperature difference term can then be divided out from both sides of the balance. After rearranging, equation 13 shows the final definition for the effective liquid conductivity

$$k_{eff} = k_{liq} + hL \qquad \textit{Eq. 13}$$

All material properties needed for calculating Ma are known from the literature, and fully displayed and cited in appendix A, but a technique for determining the proper change in temperature is needed. The theoretical maximum temperature change used is determined from considering an energy balance over the melt pool starting from the generalized energy equation 1. While the global negligible fluid motion assumption does not hold for energy balance within the melt pool some terms are still negligible by scale analysis. On the right hand side, body forces are negligible since the only potential field is gravity and low Bo dictates gravity is a negligible effect. The deviatoric stress tensor, $\boldsymbol{\tau}$, is defined using the constitutive model outlined in equation 14 and represents the viscous component of the total stress tensor. High Ma means that surface tension forces are dominant over viscous forces so the deviatoric stress term can also be neglected from the melt pool energy balance. The right hand side of the energy equation is now simplified as seen in equation 4.

$$\boldsymbol{\tau} = \mu(\nabla \boldsymbol{v} + \nabla \boldsymbol{v^T}) \qquad \textit{Eq.14}$$

On the left hand side of equation 1, the kinetic term cannot be neglected because velocity is not negligible in the melt pool. The velocity resulting from thermocapillary force scales as shown in equation 15 [33]. By using the definitions in equations 3 and 15 and applying the assumptions from scale analysis, ie. that thermocapillary is dominant over viscous and buoyant forces, the energy balance in the melt pool can be simplified to equation 16.

$$v = \frac{\partial \gamma}{\partial T}\frac{dT}{\mu} \qquad \textit{Eq. 15}$$

$$\rho \frac{D}{Dt}\left(cdT + \frac{1}{2}\left(\frac{\partial \gamma}{\partial T}\frac{dT}{\mu}\right)^2\right) = -\nabla \cdot q'' + q''' \qquad \textit{Eq. 16}$$

For this section of the analysis it is assumed that the boundaries of the molten region are adiabatic, no heat flux acts on the molten region, and the only generation term is the energy imparted by the source beam. Additionally a time step defined by equation 17 is considered to resolve the temporal derivative within the material derivative, leaving only spatial derivatives.

$$dt = \frac{L}{v_{scan}} \qquad \textit{Eq. 17}$$

If equation 16 is then integrated over melt pool volume an expression quadratic in temperature is found. By applying the quadratic formula and considering only the maximum temperature case an expression for temperature change, equation 18, is derived. In equation 18 the heat generation term uses the definition labeled equation 7. Equation 18 uses *V* to represent the melt pool volume.

$$\Delta T = \frac{-c + \sqrt{c^2 + 2\left(\frac{\partial \gamma_1}{\partial T_\mu}\right)^2 dt \int_V \frac{q'''}{\rho}}}{\left(\frac{\partial \gamma_1}{\partial T_\mu}\right)^2} \qquad \textit{Eq. 18}$$

By applying the described melt pool energy analysis Ma for each material and process are calculated as seen in table 3. Table 4 shows Nu, h, k_{eff}, as well as the ratio of k_{eff} to k_{liq} calculated using the paradigm laid out in this section of the thesis. The new k_{eff} values are the values assigned to the liquid material elements within the FEM model.

Material	$\frac{\partial \gamma}{\partial T}$ (mN/m-K)	M (Pa-s)	ΔT (K)	Nu	h (W/m²-K)	k_{eff} (W/m-K)	$\frac{k_{eff}}{k_{liq}}$
SLM Ti6Al4V	-0.28	3.25E-3	6170	4.80	3.59E6	569	19.00
EBM Ti6Al4V			12770	6.44	4.82E6	994	33.19
SLM SS316	-0.83	8.00E-3	3171	4.46	3.07E6	412	14.93
EBM SS316			7486	6.14	4.23E6	635	7.77
SLM Al7075	-0.48	1.30E-3	1134	1.50	6.83E6	269	2.73
EBM Al7075			5553	2.95	1.34E7	768	29.69
SLM IN718	-0.11	7.20E-3	6431	3.39	2.45E6	473	16.00
EBM IN718			12040	4.93	3.64E6	986	33.32

Table 4: Thermal Transport Properties for Liquid Materials at 150W Beam Power

3.1.3 Liquid Conductivity Validation

As a validation of this effective liquid conductivity approach three SLM simulations were run in Inconel 718 at beam powers of 150W, 200W and 300W, each with a scan speed of 200 mm/s, and melt pool widths were compared to experimental findings within the same research group. Table 5 shows the Ma, Nu, heat transfer coefficient, effective liquid conductivity and conductivity ratio for the three validation cases.

	ΔT (K)	**Ma**	**Nu**	**h (W/m^2-K)**	**k_{eff} (W/m-K)**	**$\frac{k_{eff}}{k_{liq}}$**
150 W	6431	4306	3.31	2.45E6	473	16.00
200 W	9198	7418	4.19	3.10E6	706	23.84
300 W	14720	13229	5.12	3.79E6	950	32.11

Table 5: Inconel Validation Measurements

The simulation measurements were taken using the procedure laid out in the results section. The experimental melt pool width values were measured by analyzing cross sectional images of the single scan solidified region taken with an optical microscope at 200 x magnification. For each power, 10 scan lines were analyzed and the results averaged to ensure proper characterization in melt pool geometry while varying process parameters. Using Matlab processing tools the melt pool width, depth, and bead height were measured in pixel count, as seen in figure 6. In the figure, the horizontal measurement denotes the melt pool width; the measurement from the horizontal upward denotes the bead height; and the measurement from the horizontal downward denotes the melt pool depth. By measuring the pixel count across the scale provided by the optical microscope images, the physical dimension is calculated.

Table 6 shows the comparison between simulation and experimental widths and depth both with and without the effective liquid conductivities calculated. The molten zone calculations do not consider material at a temperature between the solidus and liquidus

temperatures as being part of the melt pool while the molten and mushy zone does consider this material part of the melt pool.

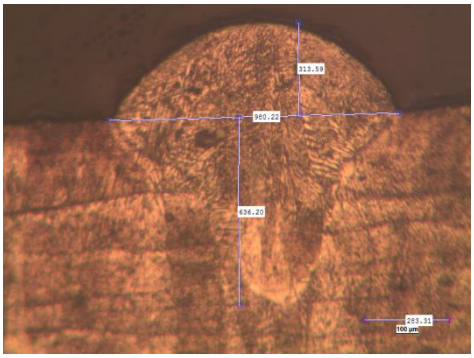

Figure 6: Cross-sectional optical microscope measurement method

In all three power cases implementing the effective liquid conductivity improves the accuracy of melt pool width and depth measurements taken from the simulation. In all three cases the depth measurement is more accurate than the width measurement after implementing the effective conductivity. Good agreement is seen for the 150W and 300W depth measurements and poorer agreement is seen for the 200W case. This could be caused by experimental measurement error since the experimental depth is larger than expected if the 150W and 300W cases are considered.

The poorer agreement in width measurement compared to depth measurement is most likely due to the non-wetting characteristic of the molten Inconel on the solidified Inconel. As the melt pool is allowed to grow in size, it tends to create a bead above the solid surface rather than spreading out. This is because of the high surface tension within the molten metal and the melt pool radius approaching the ideal droplet radius for the molten Inconel. This equilibrium radius is a function of the contact angle with the surface, and the surface tensions at the liquid-solid, liquid-vapor, and solid-vapor interfaces if they exist [28]. While more work is needed to further improve agreement in width measurements agreement between experimental and simulation depth measurements are at an acceptable level.

	Experimental width (µm)	Simulation width (µm)	Difference (%)	Experimental depth (µm)	Simulation depth (µm)	Difference (%)
With Effective Liquid Conductivity – Molten Zone						
150 W	357.2	500	39.98	215.7	220	2.00
200 W	436.1	600	37.58	280.5	230	-18.00
300 W	527.1	720	36.60	299.1	310	3.64
Without Effective Liquid Conductivity – Molten Zone						
150 W	357.2	560	56.77	215.7	275	27.49
200 W	436.1	700	60.51	280.5	340	21.21
300 W	527.1	950	80.23	299.1	460	53.79
With Effective Liquid Conductivity – Molten and Mushy Zone						
150 W	357.2	530	48.38	215.7	240	11.17
200 W	436.1	640	46.76	280.5	260	-7.31
300 W	527.1	760	44.19	299.1	330	10.33
Without Effective Liquid Conductivity – Molten and Mushy Zone						
150 W	357.2	600	67.97	215.7	300	39.08
200 W	436.1	760	74.27	280.5	360	28.34
300 W	527.1	1000	89.72	299.1	485	62.15

Table 6: Liquid Conductivity Validation

3.2 Density

Powder density values are found by multiplying the solid density value by the complement of the powder bed porosity, or the portion of the power bed volume not made up of void fluid existing between individual powder particles. A porosity of 30% is assumed in accordance with standard practices within the existing literature.

3.3 Emissivity

Emissivity properties of the powder are also affected by void fraction within the powder bed following a model derived by Sih and Barlow [27]. The Sih and Barlow model assumes grey bodies with no transmission of radiation through the body. Sih and Barlow assert that voids between powder particles have higher emission than the powder particles surrounding them and the cohesive powder bed can therefore be expected to have a higher emissivity than the solid material.

3.4 Absorptivity and Melting Zone Temperatures

Thermal absorptivity values are taken from a work published by Touloukian [34] in which radiation properties for various pure materials, binary and trinary metallic alloys are presented. The closest binary or trinary alloy group was chosen for each material considered in this work. Absorptivity values have a spectral dependence and therefore have different values for use in laser and electron beam systems since these heat sources operate at different wavelengths. Table 7 shows the absorptivity values for each material for both laser and electron beam processes. The table also includes the solidus and liquidus temperatures for each material.

Material	Absorptivity - Laser	Effective Absorptivity - EBM	Solidus Temperature (K)	Liquidus Temperature (K)
Ti6Al4V	0.65	0.73	1871	1923
SS316	0.55	0.64	1621	1706
Al7075	0.15	0.34	805	901
IN718	0.85	0.87	1533	1609

Table 7: Absorptivity, Solidus and Liquidus Temperatures for Various Engineering Materials

3.5 Other Liquid Properties

Little literature exists describing the thermophysical properties of molten metals since they can be quite daunting to accurately measure. These properties are obviously of great importance to the modeling work done in this thesis as phase transitions from powder to liquid to solid materials must be considered. Kaschnitz [35] used microsecond and millisecond pulse-heating techniques to explore thermophysical properties of Ti6Al4V up to 300K above the melting temperature. His research suggests that over the temperature range 1900K<T<2300K, liquid Ti6Al4V can be assumed to have a constant specific heat. This is a result of Kaschnitz noticing that the slope of his experimentally obtained enthalpy-temperature plot was roughly constant over the same temperature range. Boivineau [36] also used microsecond and millisecond pulse-heating techniques along with direct scanning calorimetry to explore the properties of solid and liquid Ti6Al4V from 500 to 2300 K. All thermophysical property data used within this modeling effort, with proper citations, are shown in appendix B. Miettinen [37] presents properties for liquid and SS 316L. The liquid properties for Al7075 and IN718 are found in Mills [38].

CHAPTER 4 Results

The modeling efforts described thus far have culminated in a variety of publications [39]–[41]. The main aim of the modeling efforts outlined in these publications is to compare the

behavior of different novel engineering materials built using powder bed additive processes. The first group of works [39], [40] shows the behavior of Ti6Al4V, stainless 316L and aluminum 7075 built using SLM and EBM. The most recent addition [41] further considered the behavior of Inconel 718 using the SLM process. The Inconel work also gives a more rigorous validation of the modeling setup used by comparing melt pool geometry from the simulation to measurements taken from experiments performed within by a colleague in the author's research group building single line scans from Inconel 718 powder in the SLM process.

As previously discussed in the material properties chapter of this work, previous modeling efforts from the author did not yield realistic temperatures and melt pool profiles for realistic process parameter sets. To resolve the unrealistically high temperatures seen, the author increased the beam speed and decreased the beam power to reduce the linear energy density of the source beam therefore reducing temperature and melt pool size [39], [40]. In the Inconel work [41], temperatures and melt pool geometries are increased by implementing an effective thermal conductivity. However, for that work, the procedure outlined in the material properties chapter of this work was not used. Instead a study was conducted in which liquid conductivity was increased until a saturated maximum temperature condition was reached. This means that further increase in liquid conductivity no longer reduced the maximum temperature seen in the model.

The results from decreasing linear energy density do not conform to expected melt pool sizes seen in other simulation works. Shen and Chou [42] predict that melt pools should be elliptical shaped, being larger in the scan direction (melt pool length) that in the transverse direction (melt pool width). The melt pools seen in [39], however, are circular in size. As an example. the laser Ti6Al4V melt pool length and width are both approximately 600 μm

suggesting that the melt pool length is under predicted and the melt pool width is over predicted. This type of behavior is expected for the other two materials considered in that study as well. In the Inconel study melt pool widths and depths diverge more from experimental values than then do when effective conductivity is calculated using the procedure outlined in the material properties chapter. To improve agreement a correct factor is applied to the simulation melt pool widths and depths to bring them into better agreement with experimental measurements.

The goal of the present work is to show the thermal behavior and melt pool characteristics of additive processes within all prominent engineering material types. The titanium alloy and Inconel alloy were chosen for their applicability to and common use within the aerospace industry. Stainless 316L was chosen to represent the steel class of materials since its corrosion resistance properties make it a preferred material in the biomedical industry. Aluminum 7075 was considered due to its high strength, closer than other aluminum alloys to the other classes of materials considered. Aluminum in general presents issues for the additive processes due to its thermophysical properties. The presented model matured and progressed with each publication and to be rigorous the analysis presented in the previous publications will be recreated in this thesis using the most current iteration of the FEM and thermophysical models including effective liquid conductivities.

4.1 Process Parameter Sets

Eight trials are presented in this work, one for each material class in both SLM and EBM environments. Table 8 outlines the process parameter sets for each of these trials. The goal was to have as little variation between trials as possible to say confidently that differences seen between trials are purely a result of material choice. There, however, are a few systematic differences in the parameter sets for the EBM trials and the SLM trials. The electron beam used

in EBM is capable of penetrating deeper into the powder bed than the laser used in SLM. For this reason the penetration depth in all EBM trials is larger than in SLM. Additionally, EBM includes an initial preheat and sintering of the powder bed after the addition of each layer. This is not a standard practice in the laser processes. For this reason, the ambient temperature in the EBM trials is elevated while the ambient temperature in the SLM trials is room temperature. The preheat temperature for the titanium, steel and Inconel trials are derived from Shen and Chou's [18] work in titanium built by EBM. The steel and Inconel preheat temperatures were taken to be the same as titanium for the sake of consistency. This preheat temperature is above the liquidus temperature for Al 7075 so an adjustment was made for the aluminum EBM trial. The preheat temperature for the aluminum was found by assuming the same ratio of preheat temperature to liquidus temperature used in titanium could be applied to aluminum. The beam power and beam scan speed needed to be adjusted for the aluminum trials as well due to aluminum's thermophysical properties. Aluminum has both a high thermal conductivity and a low absorptivity. The low absorptivity means that little energy is transferred from the source beam into the aluminum powder bed. The high conductivity means that whatever energy is transferred into the powder bed is then rapidly diffused into the rest of the powder bed, inhibiting temperatures high enough to consistently melt the aluminum powder. By increasing the beam power more energy is supplied to the powder to increase the temperature. Reducing scan speed means that the area of the powder bed under the beam is subjected to the energy input of the beam for a greater period of time to increase the temperature. Even with these two adjustments the aluminum trials show much smaller melt pool geometries than the other materials considered.

Process Parameter	Laser Ti, IN and SS	Laser Al	EBM Ti, IN and SS	EBM Al
Ambient Temperature	298 K	298 K	1033 K	471 K
Effective Beam Diameter	200 µm	200 µm	200 µm	200 µm
Penetration Depth	100 µm	100 µm	200 µm	200 µm
Beam Power	150 W	400 W	150 W	400 W
Powder Bed Porosity	0.3	0.3	0.3	0.3
Beam Scan Velocity	0.2 m/s	0.2 m/s	2 m/s	2 m/s

Table 8: Process parameter selection

4.2 Temperature Contours

Figures 7 and 8 show temperature contour plots for each of the trials performed. For all temperature data presented in this section of the thesis the models were queried at a simulation time of 9 ms. The simulation time was chosen arbitrarily and represents a time step in the middle of the simulation. Both figures show the FEM model cross sectioned about the beam line of action so that only the bottom half of each block is shown. In figure 6 the front, left face of each block shows the top of the powder layer and the top, right face show temperature propagation into the depth of the model through the powder and solid layers into the base plate. Figure 7 shows just a top down view of the bottom half of the model looking at the top of the powder bed. Figure 7 compares all trials on a common temperature scale while figure 7 shows each trail with its unique temperature scale.

In considering figure 6 one can observe that titanium and Inconel reach higher maximum temperatures and have broader heat affected zones than the steel. The aluminum trials shows barely any temperature elevation due to the reasons previously discussed. The thermophysical property differences between titanium, steel and Inconel also explain the differences seen in temperature distribution. Titanium has the lowest thermal conductivity of the four material classes considered but also has a relatively high absorptivity, with Inconel being the only material with higher absorptivity. In much the same way it was argued that low absorptivity and

high conductivity reduce the ability of aluminum to reach elevated temperature it follows that high absorptivity and low conductivity enhances titanium's ability to reach elevated temperature. While Inconel has a higher conductivity than titanium, almost the same as steel, it also has the highest absorptivity of the materials considered. For this reason Inconel is still able to reach the same elevated temperatures as seen in titanium even though it is more effectively dissipating heat away from under the beam spot.

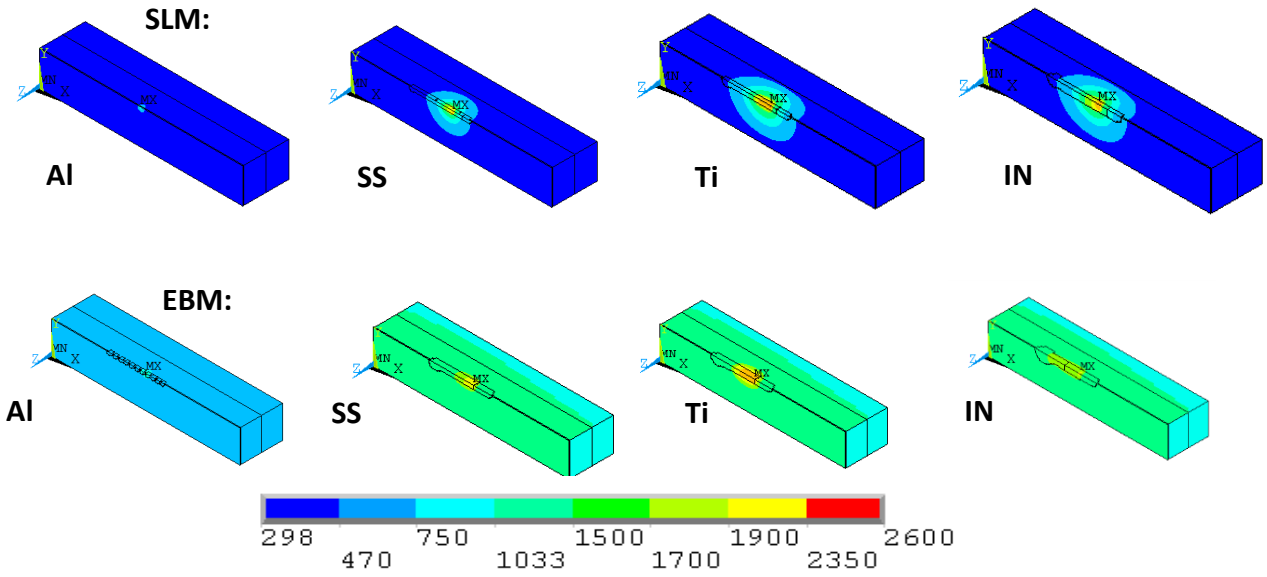

Figure 7: Temperature contour maps on common scale in Kelvin

In figure 8, particularly the EBM trials, there exists a trailing effect in the temperature contours where elevated temperatures are seen more to the left, or previously scanned, part of the block than on the right side which is yet to be scanned. This is because the solid thermal conductivity for all materials is greater than the powder conductivity so heat is preferentially transferred into the already solidified region instead of heating up the region leading the beam scan. The temperature profiles presented in figure 7 are symmetric above the beam line of action, represented by the top line of each contour map.

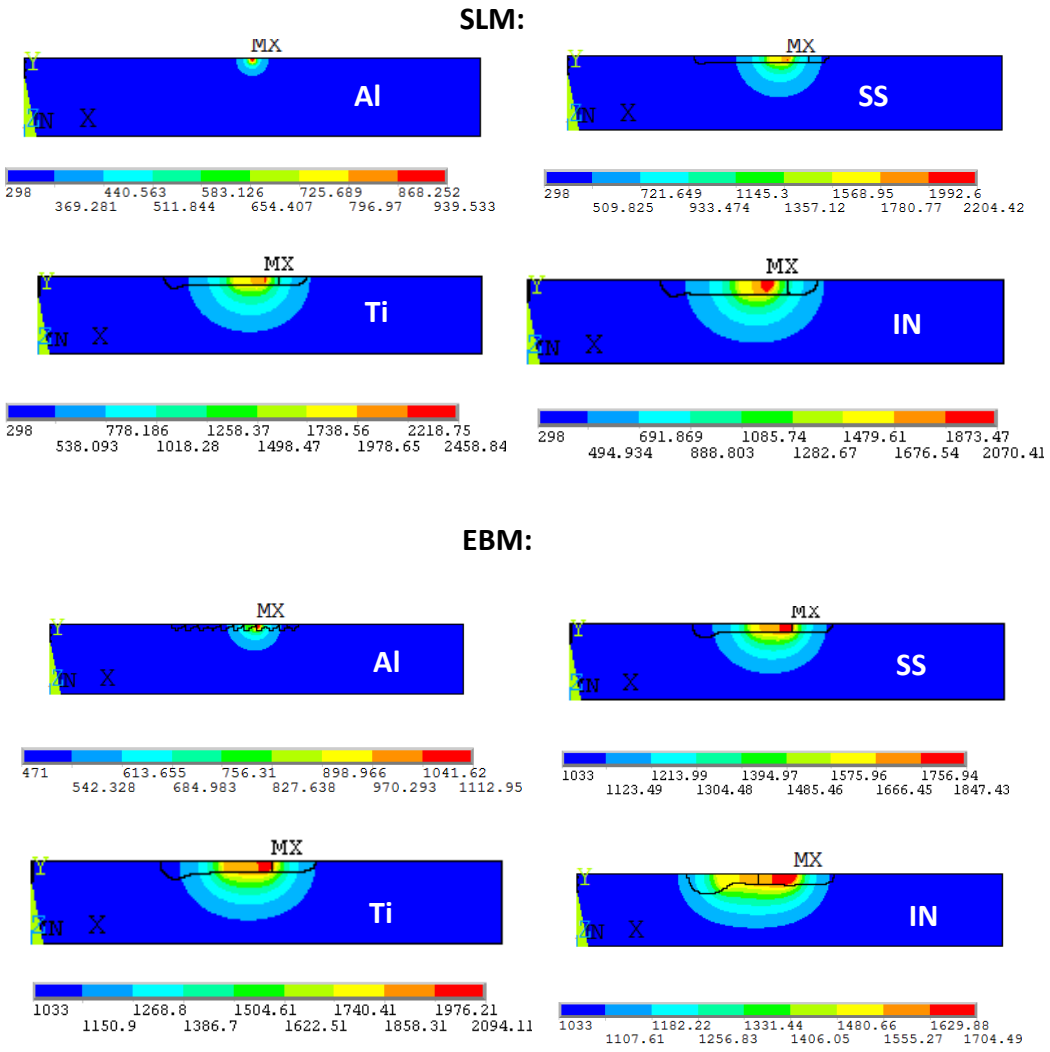

Figure 8: Temperature contour maps with unique scales in Kelvin

Melt pool geometry plays an important role in determining the quality of the final built part. In order to create a final part absent of voids and within proper dimensional tolerances it is important to understand how the melt pool is formed and sustained throughout the build. Determining the melt pool geometry, and subsequently the solidified region geometry provides a good way to validate the developed model. Transiently gathering temperature data experimentally during part builds can be a daunting task, and as shown by Price [43] does not provide meaningfully accurate data. A better validation technique is to compare melt pool depth and width measurements gathered experimentally to simulated results.

4.3 Melt Pool Geometry

4.3.1 Element Plots

In the presented model there are two techniques for determining the melt pool geometry. A first, more qualitative, approach is to consider the phase change phenomena present within the model as previously described in the modeling set up chapter. The element plots shown in figure 9 show the final element definitions at the end of the simulation and show the phase change history of the model. In this figure the purple region signifies a region that was powder for the duration of the simulation. The orange region is a region that was melted at some point during the simulation and then resolidified before the end of the simulation. The red region is the region still molten at the end of the simulation. The cyan region is the region that started the simulation as solid material and was not melted at any point during the simulation and the dark blue region denotes the build plate.

In the aluminum SLM trial no phase change is recorded by considering the element plot. However, later analysis shows that proper temperatures are developed to create a molten region, the region is just smaller than the element size within the model. This discrepancy leads the author to use the second melt pool geometry measurement technique, explained later. In the aluminum EBM trial there is still not a high enough temperature and strong enough heat input to sustain a consistent melt pool, as seen in the other materials. The author did not further augment the process parameters used in either aluminum trial because doing so would bring the parameter sets out of realistic power and scan speed ranges.

The titanium and Inconel trials exhibit broader melt pools, as expected, since they were capable of reaching higher temperatures due to their thermophysical properties. The circular region to the left of the melt pool histories in the steel, titanium and Inconel EBM trials can be

explained by the conductivity difference between solid and powder materials as well. These melt pools formed at the beginning of the simulation where no solidified material existed in the top layer of the model. For this reason all heat was equally dissipated radially allowing for a circular region to reach the liquidus temperature. After the region solidified it acted as a heat sink to draw energy back into the previously scanned portion of the scan line causing an elongation of the melt pool.

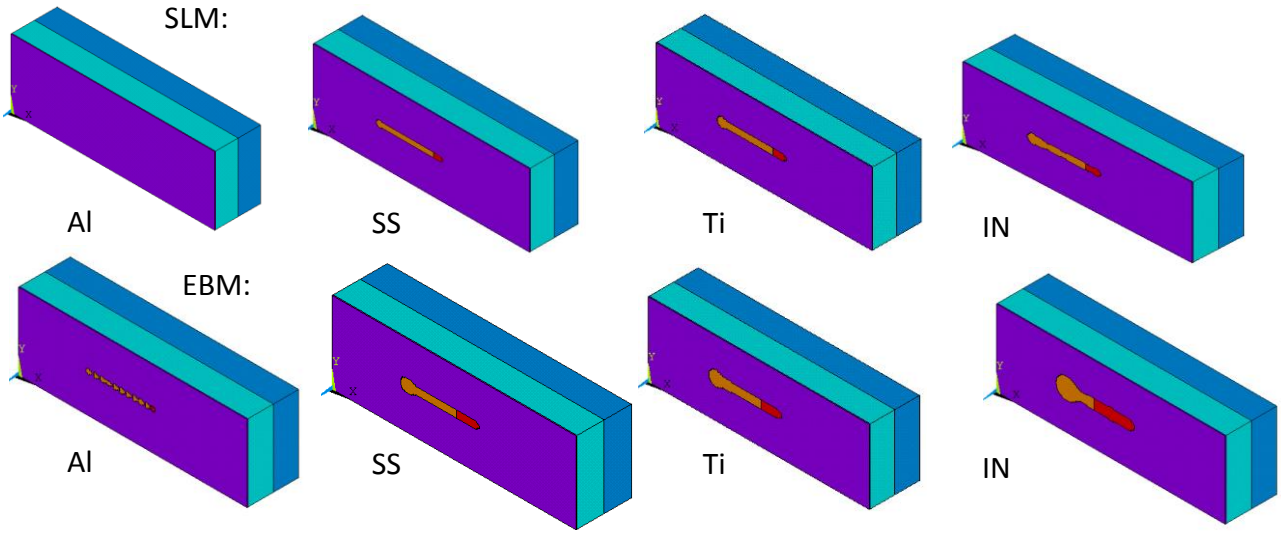

Figure 9: Element plot melt pool geometry characterization

4.3.2 Thermal Maps

The second, more meaningful, method of determining melt pool geometry is by considering the thermal data taken from the model. Figures 10-12 show graphically the temperature data outlined in figures 7 and 8 pictorially. This data also corresponds to simulation time of 9 ms. The data was taken by mapping the temperature profiles onto a set of three lines, one in the x, y, and z direction, intersecting the beam center. The x direction data, seen in figure 10, shows the temperature data on a horizontal line passing through the center of the beam line of action. The y direction data, figure 11, shows the temperature distribution along a vertical line intersecting the x direction line at the beam center. The z direction data, figure 12, shows the

temperature along a line projected depthwise from the intersection point of the x and y lines. The solidus and liquidus temperatures are also plotted on these three figures as reference and to aid in identifying melt pool measurements. Please note that the horizontal axis values on these three figures are relative in nature and all measurements need to be made by subtracting between two points on the horizontal chart axis. In each of these three charts, continuous temperature curves are presented. These curves are taken by interpolating between temperature values at the nodes along the temperature mapping lines in the model.

The melt pool length was determined by calculating the x direction distance between intersection points of the temperature profile of interest and the corresponding solidus line of the material. The technique described here can be performed by comparing against either the solidus or the liquidus line, however, validation trials showed better agreement when considering the solidus line so all data presented from this analysis compares against the solidus temperatures of the materials and represents the entire mushy region, not just the purely liquid region. In alloyed materials the different composition elements melt at different melting temperatures so the melting over the alloy occurs over a temperature range between the solidus and liquidus temperatures. This is contrary to a pure material that melts at a specific melting temperature. Temperature profiles in the scan direction are shaped differently in EBM and laser melting cases. This is a result of the differences in effective liquid conductivity and effective powder conductivity across build processes. Both effective conductivity values are higher in EBM than in laser melting. The higher effective liquid conductivity results in longer melt pool lengths and a flatter thermal profile above the liquidus temperature. The lower maximum temperature and flatter thermal profiles in the EBM case also suggest that less thermal stresses will be seen in a part built by EBM than in a part built by laser melting. The higher effective powder

conductivity, along with the higher ambient temperature, results in a shallower slope on the thermal profile ahead of the beam spot.

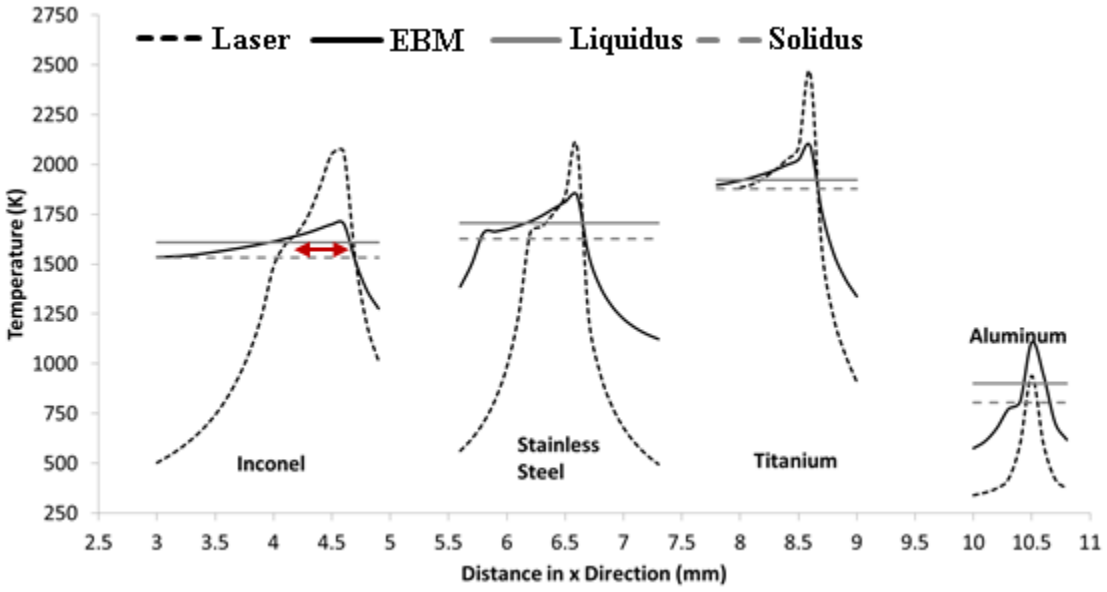

Figure 10: X direction temperature data – Melt pool length characterization

The melt pool width is determined by the same method expect with respect to the y direction distance, not the x direction distance. For the melt pool depth there is only one intersection point between the temperature profile and the corresponding solidus line. For this measurement the distance between the intersection point and the start of the temperature profile needs to be considered. On each figure a red arrow is included to show a representative measurement. Table 9 shows the melt pool length, width and depth measurements taken for each of the eight trials considered.

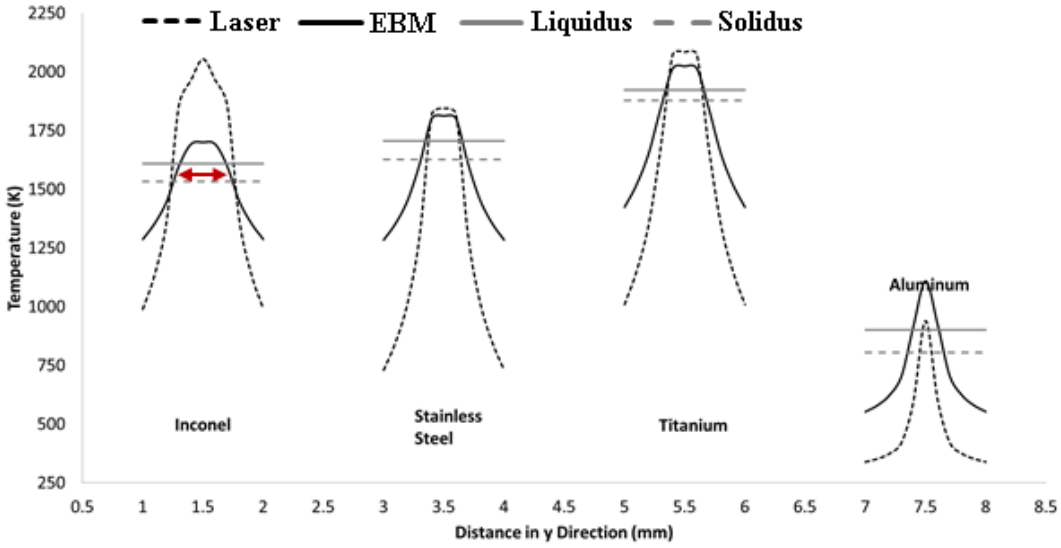

Figure 11: Y direction temperature data – Melt pool width characterization

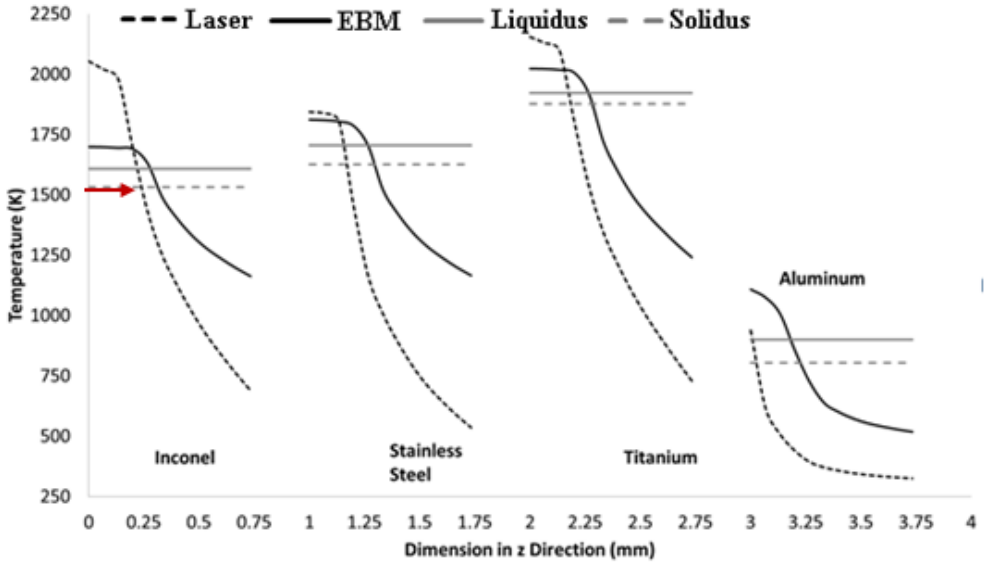

Figure 12: Z direction temperature data – Melt pool depth characterization

	Mushy Region Length (μm)	Mushy Region Width (μm)	Mushy Region Depth (μm)
	Molten Zone		
Inconel Laser	600	500	220
Inconel EBM	700	460	275
Stainless Steel Laser	300	300	150
Stainless Steel EBM	450	350	260
Titanium Laser	450	300	175
Titanium EBM	550	300	275
Aluminum Laser	50	50	10
Aluminum EBM	200	200	180
	Molten and Mushy Zone		
Inconel Laser	680	530	240
Inconel EBM	1400	530	310
Stainless Steel Laser	480	320	175
Stainless Steel EBM	900	400	300
Titanium Laser	650	350	190
Titanium EBM	900	400	290
Aluminum Laser	100	100	30
Aluminum EBM	250	300	225

Table 9: Melt pool geometry in three directions

CHAPTER 5 Conclusions

Through the creation of a transient thermal FEM model the author was able to compare the thermal transport and phase change behavior of four principle engineering material classes across two main categories of powder bed AM processes. Both qualitative and quantitative comparisons are presented and general trends between material classes and process type are discussed. Titanium and Inconel, compared to the other materials built with the same build parameters, reach higher maximum temperatures and create larger melt pools in the three dimensions considered. This is a result of the thermal conductivity of these two materials in powder form being less than the other materials in powder form. Additionally these two

materials have higher thermal absorptivities, meaning energy is more effectively transmitted form the source beam into the powder bed, than the other two materials. Aluminum, even with adjusted process parameter sets, is quite difficult to build additively.

Modeling efforts were simplified and computational resources relaxed by using effective thermophysical properties when required to mask more complicated physical phenomena present within the actual system. An effective powder conductivity value is used to encapsulate the thermal transport, conduction, convection and radiation, occurring at the inter-particle level within the melt pool. An effective liquid conductivity encapsulates fluid motion within the melt pool and its effects on thermal transport. A rigorous derivation and physical motivation for the use of these effective properties was presented. Through the material and process comparisons included the author concludes that process parameter sets need to be tailored to each material and process pair to ensure consistent melt pool characteristics and desirable final part properties. Additionally the author concedes there are some melt pool flow characteristics, particularly the non-wetting phenomenon occurring in larger melt pools, which an effective properties approach does not reconcile with.

Further efforts must be dedicated toward fully understanding the governing physics behind the non-wetting problem and adjustments to the current modeling paradigm must be proposed, either through changes to the effective properties definition given in this work or through the coupling of CFD analyses to FEM analyses. Non-wetting may be included in the effective liquid conductivity derivation if the Young-Laplace equation is considered. A Young-Laplace analysis yields the wetting angle at the solid-liquid interface. This can be used, along with a calculated melt pool volume, to determine the bead height above the melt pool and the required reduction in melt pool width.

5.1 Contributions to the Community

Through this work the author was able to broaden the base of powder bed AM literature by considering and comparing many novel engineering materials. Since the materials analyzed here can be considered representative of other alloys within their classes the behavior of many alloys can be predicted using the methodology laid out in this thesis. Furthermore, while effective powder conductivity values are present within many studies in the literature, this work is the first, to the author's knowledge, to consider an effective liquid conductivity. Through the author's validation trials in Inconel 718 at various powers the author has shown better agreement between experimental and simulation melt pool measurements than without use of an effective liquid conductivity. There is still, however, further room for improvement in the melt pool model. A coupled CFD representing the mass transport within the melt pool may better predict the melt pool size. It may also be possible to encapsulate the non-wetting phenomenon, seen between liquid and solid materials in the experimental trials, as an additional term in the effective liquid conductivity derivation.

REFERENCES

[1] D. L. Bourell, J. J. Beaman, M. C. Leu, and D. W. Rosen, "A Brief History of Additive Manufacturing and the 2009 Roadmap for Additive Manufacturing: Looking Back and Looking Forward," *US-TURKEY Work. Rapid Technol. Sept. 24, 2009*, pp. 5–11, 2009.

[2] J.-P. Kruth, M. C. Leu, and T. Nakagawa, "Progress in Additive Manufacturing and Rapid Prototyping," *CIRP Ann. - Manuf. Technol.*, vol. 47, no. 2, pp. 525–540, 1998.

[3] F. P. W. Melchels, J. Feijen, and D. W. Grijpma, "A review on stereolithography and its applications in biomedical engineering," *Biomaterials*, vol. 31, no. 24, pp. 6121–6130, 2010.

[4] B. Vayre, F. Vignat, and F. Villeneuve, "Metallic additive manufacturing: state-of-the-art review and prospects," *Mech. Ind.*, vol. 13, no. 2, pp. 89–96, May 2012.

[5] P. F. Jacobs, *Rapid Prototyping & Manufacturing: Fundamentals of StereoLithography*, 1st ed. New York, NY: McGraw-Hill, 1992.

[6] S.-H. Ahn, M. Montero, D. Odell, S. Roundy, and P. K. Wright, "Anisotropic material properties of fused deposition modeling ABS," *Rapid Prototyp. J.*, vol. 8, no. 4, pp. 248–257, 2002.

[7] E. Sachs, M. Cima, P. Williams, D. Brancazio, and J. Cornie, "Three Dimensional Printing: Rapid Tooling and Prototypes Directly from a CAD Model," *J. Eng. Ind.*, vol. 114, no. 4, pp. 481–4888, 1992.

[8] B. J. de Gans, P. C. Duineveld, and U. S. Schubert, "Inkjet Printing of Polymers: State of the Art and Future Developments," *Adv. Mater.*, vol. 16, no. 3, pp. 203–213, 2004.

[9] K. V. Wong and A. Hernandez, "A Review of Additive Manufacturing," *ISRN Mech. Eng.*, vol. 2012, pp. 1–10, 2012.

[10] S. H. Huang, P. Liu, A. Mokasdar, and L. Hou, "Additive manufacturing and its societal impact: A literature review," *Int. J. Adv. Manuf. Technol.*, vol. 67, no. 5–8, pp. 1191–1203, 2013.

[11] J.-P. Kruth, G. Levy, F. Klocke, and T. H. C. Childs, "Consolidation phenomena in laser and powder-bed based layered manufacturing," *CIRP Ann. - Manuf. Technol.*, vol. 56, no. 2, pp. 730–759, Jan. 2007.

[12] J.-P. Kruth, P. Mercelis, J. Van Vaerenbergh, L. Froyen, and M. Rombouts, "Binding mechanisms in selective laser sintering and selective laser melting," *Rapid Prototyp. J.*, vol. 11, no. 1, pp. 26–36, 2005.

[13] X. C. Wang, T. Laoui, J. Bonse, J. P. Kruth, B. Lauwers, and L. Froyen, "Direct Selective Laser Sintering of Hard Metal Powders: Experimental Study and Simulation," *Int. J. Adv. Manuf. Technol.*, vol. 19, no. 5, pp. 351–357, Mar. 2002.

[14] M. . Khaing, J. Y. . Fuh, and L. Lu, "Direct metal laser sintering for rapid tooling: processing and characterisation of EOS parts," *J. Mater. Process. Technol.*, vol. 113, no. 1–3, pp. 269–272, Jun. 2001.

[15] EOS, “EOSINT M Technology for Direct Metal Laser-Sintering (DMLS).” pp. 1–53, 2007.

[16] Arcam, “Arcam Q10 Product Literature.” .

[17] M. A. Larosa, A. L. Jardini, C. A. D. C. Zavaglia, P. Kharmandayan, D. R. Calderoni, and R. Maciel Filho, “Microstructural and Mechanical Characterization of a Custom-Built Implant Manufactured in Titanium Alloy by Direct Metal Laser Sintering,” *Adv. Mech. Eng.*, vol. 2014, pp. 1–8, 2014.

[18] N. Shen and K. Chou, “Thermal Modeling of Electron Beam Additive Manufacturing Process: Powder Sintering Effects,” *... Int. Manuf. ...*, pp. 1–9, 2012.

[19] B. Song, S. Dong, H. Liao, and C. Coddet, “Process parameter selection for selective laser melting of Ti6Al4V based on temperature distribution simulation and experimental sintering,” *Int. J. Adv. Manuf. Technol.*, vol. 61, no. 9–12, pp. 967–974, Dec. 2011.

[20] I. A. Roberts, C. J. Wang, R. Esterlein, M. Stanford, and D. J. Mynors, “A three-dimensional finite element analysis of the temperature field during laser melting of metal powders in additive layer manufacturing,” *Int. J. Mach. Tools Manuf.*, vol. 49, no. 12–13, pp. 916–923, Oct. 2009.

[21] A. Simchi, “Direct laser sintering of metal powders: Mechanism, kinetics and microstructural features,” *Mater. Sci. Eng. A*, vol. 428, no. 1–2, pp. 148–158, Jul. 2006.

[22] B. Vayre, F. Vignat, and F. Villeneuve, “Identification on some design key parameters for additive manufacturing: application on Electron Beam Melting,” *Procedia CIRP*, vol. 7, pp. 264–269, 2013.

[23] S. Kolossov, E. Boillat, R. Glardon, P. Fischer, and M. Locher, “3D FE simulation for temperature evolution in the selective laser sintering process,” *Int. J. Mach. Tools Manuf.*, vol. 44, no. 2–3, pp. 117–123, Feb. 2004.

[24] L. Dong, a. Makradi, S. Ahzi, and Y. Remond, “Three-dimensional transient finite element analysis of the selective laser sintering process,” *J. Mater. Process. Technol.*, vol. 209, no. 2, pp. 700–706, Jan. 2009.

[25] A. N. Arce, *Thermal Modeling and Simulation of Electron Beam Melting for Rapid Prototyping on Ti6Al4V Alloys*. 2012.

[26] S. Rouquette, J. Guo, and P. Le Masson, “Estimation of the parameters of a Gaussian heat source by the Levenberg-Marquardt method: Application to the electron beam welding,” *Int. J. Therm. Sci.*, vol. 46, no. 2, pp. 128–138, 2007.

[27] S. S. Sih and J. W. Barlow, “The Prediction of the Emissivity and Thermal Conductivity of Powder Beds,” *Part. Sci. Technol.*, vol. 22, no. 4, pp. 427–440, Oct. 2004.

[28] A. Faghri and Y. Zhang, *Transport Phenomena in Multiphase Systems*. Burlington, MA: Elsevier, 2006.

[29] Y. Li and D. Gu, “Parametric analysis of thermal behavior during selective laser melting additive manufacturing of aluminum alloy powder,” *Mater. Des.*, vol. 63, pp. 856–867, Nov. 2014.

[30] G. R. Hadley, “Thermal Conductivity of Packed Metal Powders,” *Int. J. Heat Mass Transf.*, vol. 29, no. 6, pp. 909–920, 1986.

[31] J. S. Agapiou and M. F. DeVries, “An Experimental Determination of the Thermal Conductivity of a 304L Stainless Steel Powder Metallurgy Material,” *J. Heat Transfer*, vol. 111, no. 2, pp. 281–286, 1989.

[32] J. Straub, “The role of surface tension for two-phase heat and mass transfer in the absence of gravity,” *Exp. Therm. Fluid Sci.*, vol. 9, no. 3, pp. 253–273, 1994.

[33] B. C. Lee, “Temperature Gradient Driven Marangoni Convection of a Spherical Liquid-Liquid Interface under Reduced Gravity Conditions,” University of Toronto, 1999.

[34] Y. Touloukian and D. DeWitt, “Thermophysical Properties of Matter-The TPRC Data Series. Volume 7. Thermal Radiative Properties-Metallic Elements and Alloys,” 1972.

[35] E. Kaschnitz, P. Reiter, and J. L. Mcclure, “Thermophysical Properties of Solid and Liquid 90Ti – 6Al – 4V in the Temperature Range from 1400 to 2300 K Measured by Millisecond and Microsecond Pulse-Heating Techniques 1,” vol. 23, no. 1, pp. 267–275, 2002.

[36] M. Boivineau, C. Cagran, D. Doytier, V. Eyraud, M.-H. Nadal, B. Wilthan, and G. Pottlacher, “Thermophysical Properties of Solid and Liquid Ti-6Al-4V (TA6V) Alloy,” *Int. J. Thermophys.*, vol. 27, no. 2, pp. 507–529, Mar. 2006.

[37] J. Miettinen, “Calculation of Solidification-Related Thermophysical Properties for Steels,” vol. 28, no. April, pp. 281–297, 1997.

[38] K. C. Mills, *Recommended Values of Thermophysical Properties for Selected Commercial Alloys*. Woodhead Publishing, 2002.

[39] J. Romano, L. Ladani, J. Razmi, and M. Sadowski, “Temperature Distribution and Melt Geometry in Laser and Electron-Beam Melting Processes–A Comparison among Common Materials,” *Addit. Manuf.*, vol. 8, pp. 1–11, 2015.

[40] J. Romano, L. Ladani, and M. Sadowski, “Thermal Modeling of Laser Based Additive Manufacturing Processes within Common Materials,” *Procedia Manuf.*, vol. 1, pp. 238–250, 2015.

[41] J. Romano, L. Ladani, and M. Sadowski, “Laser additive melting and solidification of Inconel 718: finite element simulation and experiment,” *J. Met.*, 2015.

[42] N. Shen and K. Chou, “NUMERICAL THERMAL ANALYSIS IN ELECTRON BEAM ADDITIVE,” pp. 774–784, 2012.

[43] S. Price, J. Lydon, K. Cooper, and K. Chou, “Experimental Temperature Analysis of Powder-Based Electron Beam Additive Manufacturing,” pp. 162–173, 2013.

[44] The Aluminum Association Inc., “International Alloy Designations and Chemical Composition Limits for Wrought Aluminum and Wrought Aluminum Alloys,” *Alum. Assoc. Arlington, Virginia*, no. April 2006, p. 28, 2006.

[45] Special Metals, “INCONEL alloy 718,” 2014.

[46] SAE International, “AMS5524L Steel, Corrosion and Heat-Resistant, Sheet, Strip and Plate, 18Cr-13Ni-2.5Mo (SAE 30316), Solution Heat Treated.” 2014.

[47] ASTM International, “ASTM F1108-14, Standard Specification for Titanium-6Aluminum-4Vandanium Alloy Casting for Surgical Implants (UNS R56406).” West Conshohocken, PA, 2014.

[48] Y. Touloukian, R. Powell, C. Ho, and P. Klemens, “Thermophysical Properties of Matter-The TPRC Data Series. Volume 1. Thermal Conductivity-Metallic Elements and Alloys,” 1970.

[49] Y. Touloukian and E. Buyco, “Thermophysical Properties of Matter-The TPRC Data Series. Volume 4. Specific Heat-Metallic Elements and Alloys,” 1971.

[50] G. Chahine, “Application of digital engineering in the development of a bio-adaptable dental implant,” 2011.

APPENDIX A: Chemical composition of materials of interest

Al7075 [44]

Element	Composition, wt %
Silicon (Si)	0.40
Iron (Fe)	0.50
Copper (Cu)	1.20 – 2.00
Magnesium (Mg)	0.30
Manganese (Mn)	2.10 – 2.90
Chromium (Cr)	0.18 – 0.28
Zinc (Zn)	5.10 – 6.10
Titanium (Ti)	0.20
Aluminum (Al)	Balance

Inconel 718 [45]

Element	Composition, wt %
Nickel (plus Cobalt) (Ni, Co)	50.00 - 55.00
Chromium (Cr)	17.00 - 21.00
Iron (Fe)	Balance
Niobium (plus Tantalum) (Nb, Ta)	4.75 - 5.50
Molybdenum (Mo)	2.80 – 3.30
Titanium (Ti)	0.65 – 1.15
Aluminum (Al)	0.20 – 0.80
Cobalt (Co)	1.00 max
Carbon (C)	0.08 max
Manganese (Mn)	0.35 max
Silicon (Si)	0.35 max
Phosphorus (P)	0.015 max
Sulfur (S)	0.015 max
Boron (B)	0.006 max
Copper (Cu)	0.30 max

Stainless Steel 316 [46]

Element	Composition, wt %
Nickel (Ni)	12.00
Chromium (Cr)	17.00
Molybdenum (Mo)	2.50
Iron (Fe)	Balance
Silicon (Si)	1.00
Manganese (Mn)	2.00
Carbon (C)	0.080
Phosphorus (P)	0.045
Sulfur (S)	0.030

Ti6Al4V [47]

Element	Composition, wt %
Aluminum (Al)	5.50 - 6.75
Vanadium (V)	3.50 – 4.50
Carbon (C)	< 0.10
Iron (Fe)	< 0.30
Oxygen (O)	< 0.20
Nitrogen (N)	< 0.05
Hydrogen (H)	< 0.015
Titanium(Ti)	Balance

APPENDIX B: Thermophysical properties

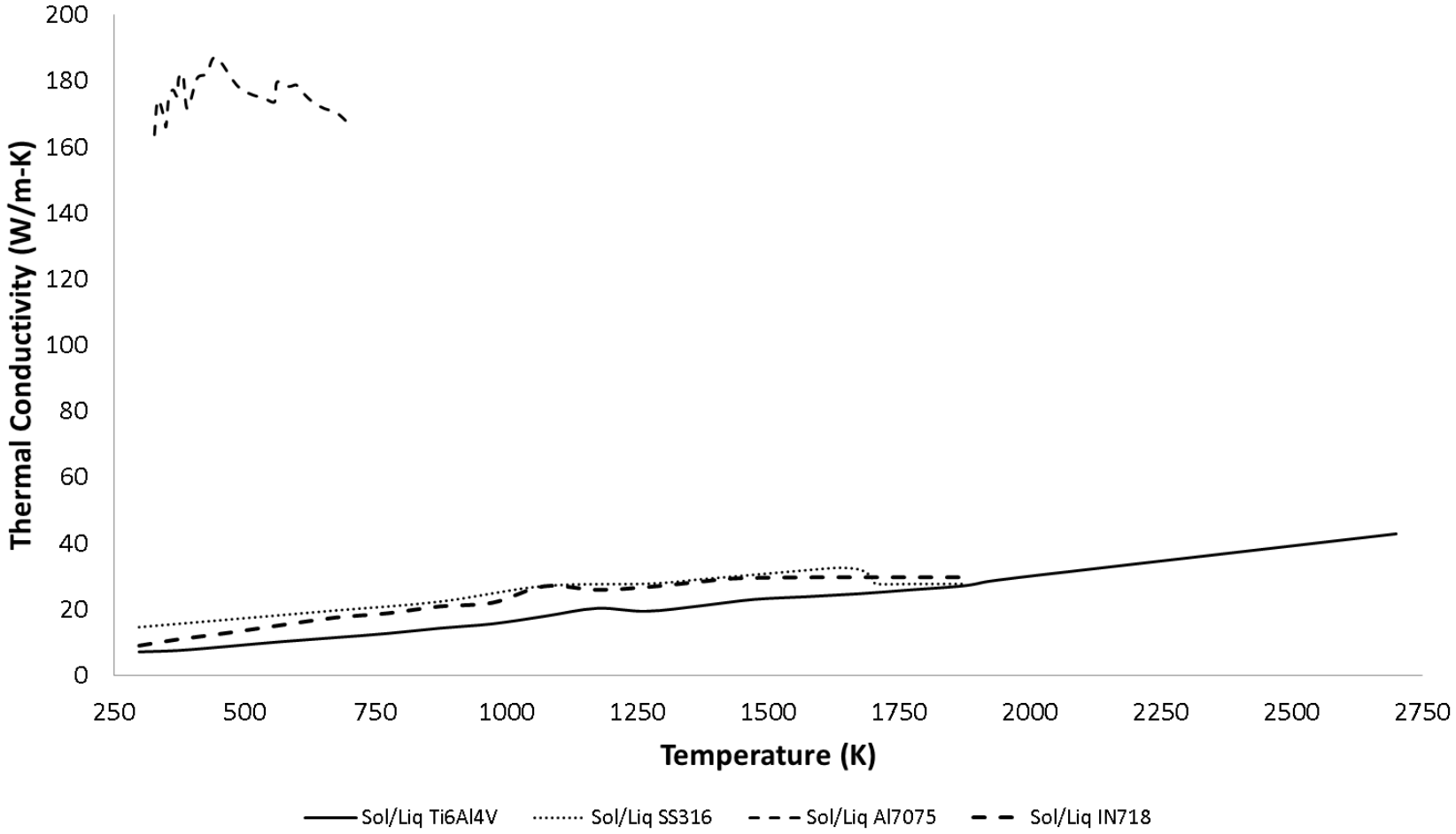

[35]–[38], [48]

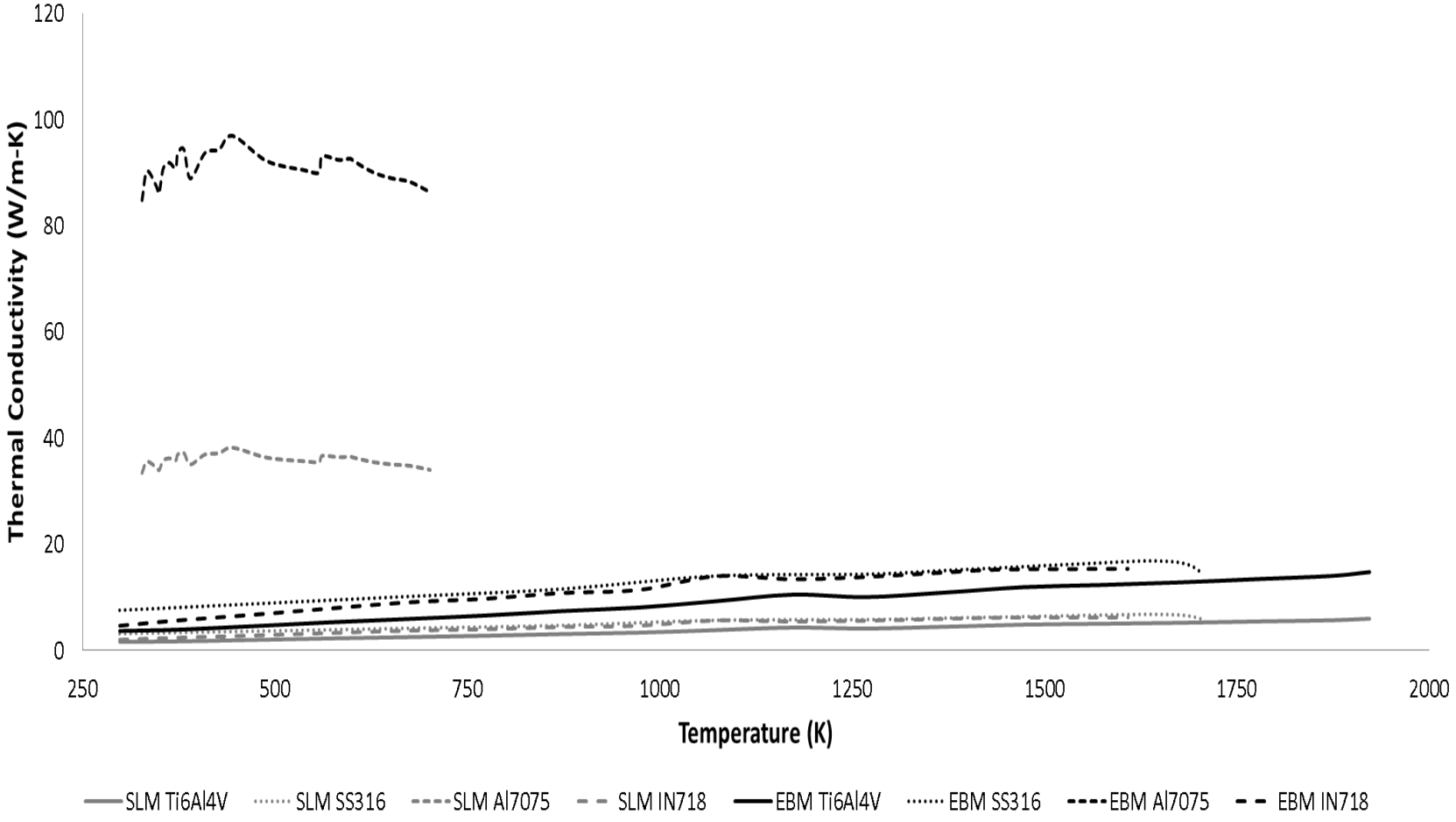
120
100
80
60
40
20
0
Thermal Conductivity (W/m-K)
250
500
750
1000
1250
1500
1750
2000
Temperature (K)
SLM Ti6Al4V
SLM SS316
SLM Al7075
SLM IN718
EBM Ti6Al4V
EBM SS316
EBM Al7075
EBM IN718

[30], [31], [35]–[38], [48]

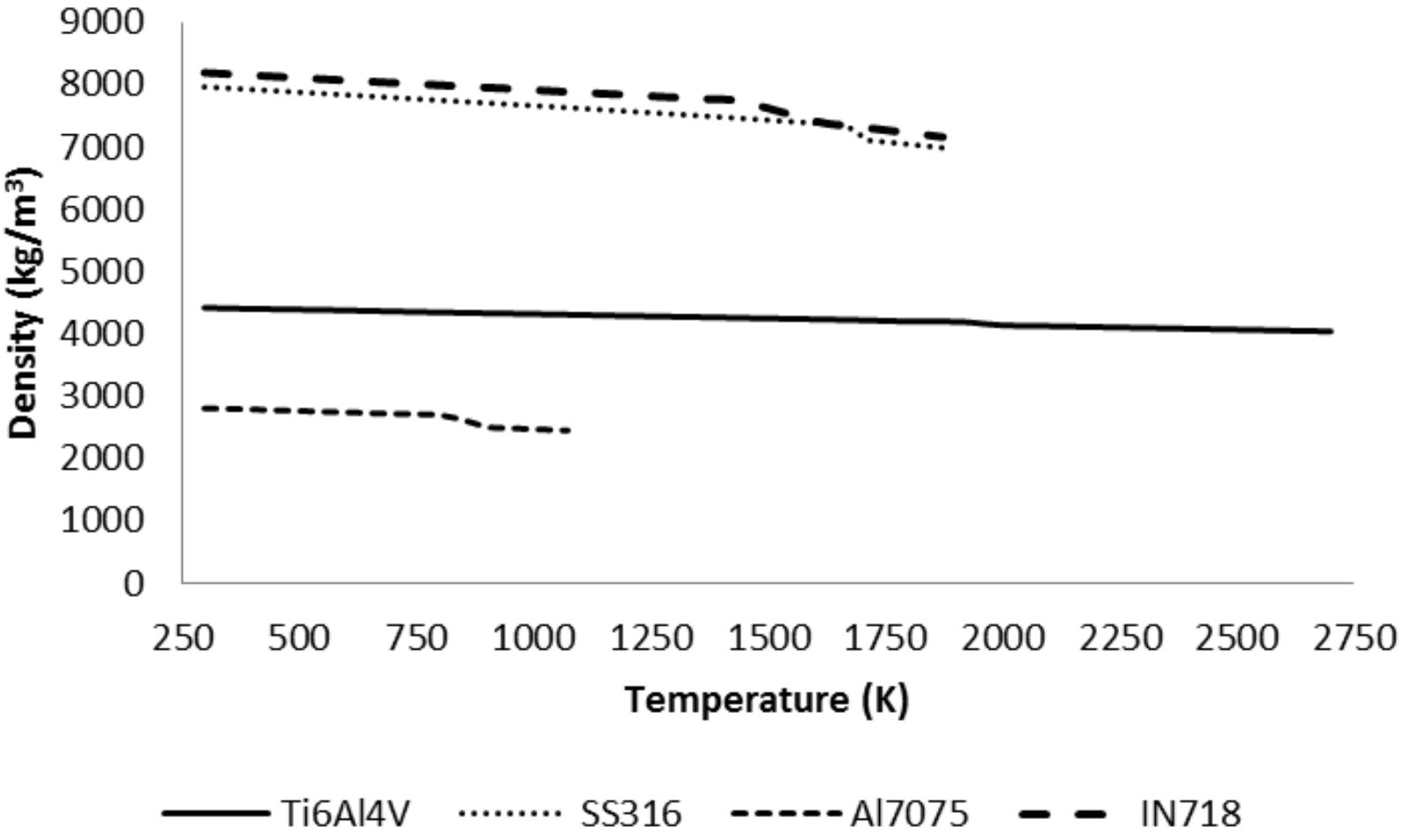
9000
8000
7000
6000
5000
4000
3000
2000
1000
0
Density (kg/m³)
250
500
750
1000
1250
1500
1750
2000
2250
2500
2750
Temperature (K)
Ti6Al4V
SS316
Al7075
IN718

[38]

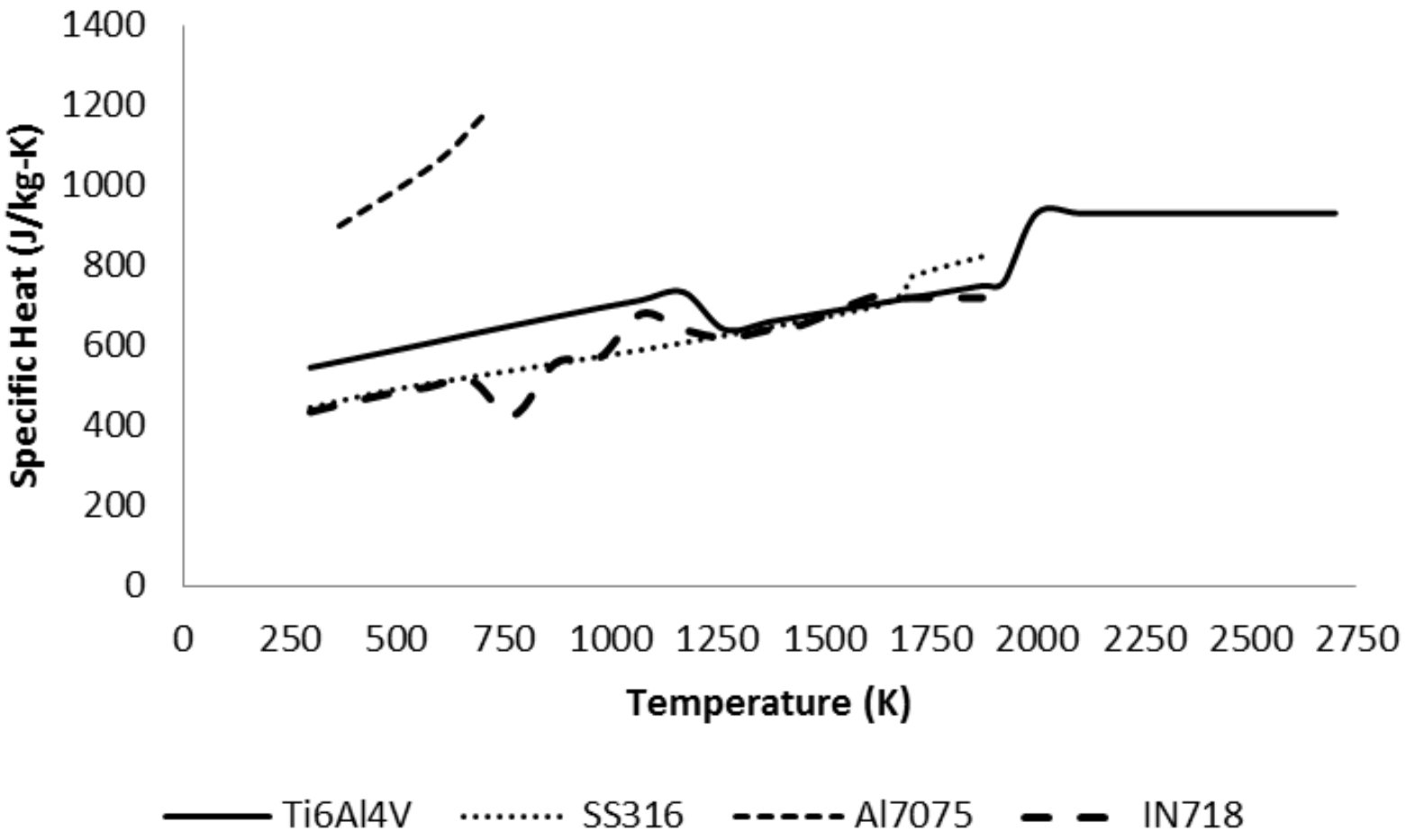
1400
1200
1000
800
600
400
200
0
Specific Heat (J/kg-K)
0
250
500
750
1000
1250
1500
1750
2000
2250
2500
2750
Temperature (K)
Ti6Al4V
SS316
Al7075
IN718

[38], [49]

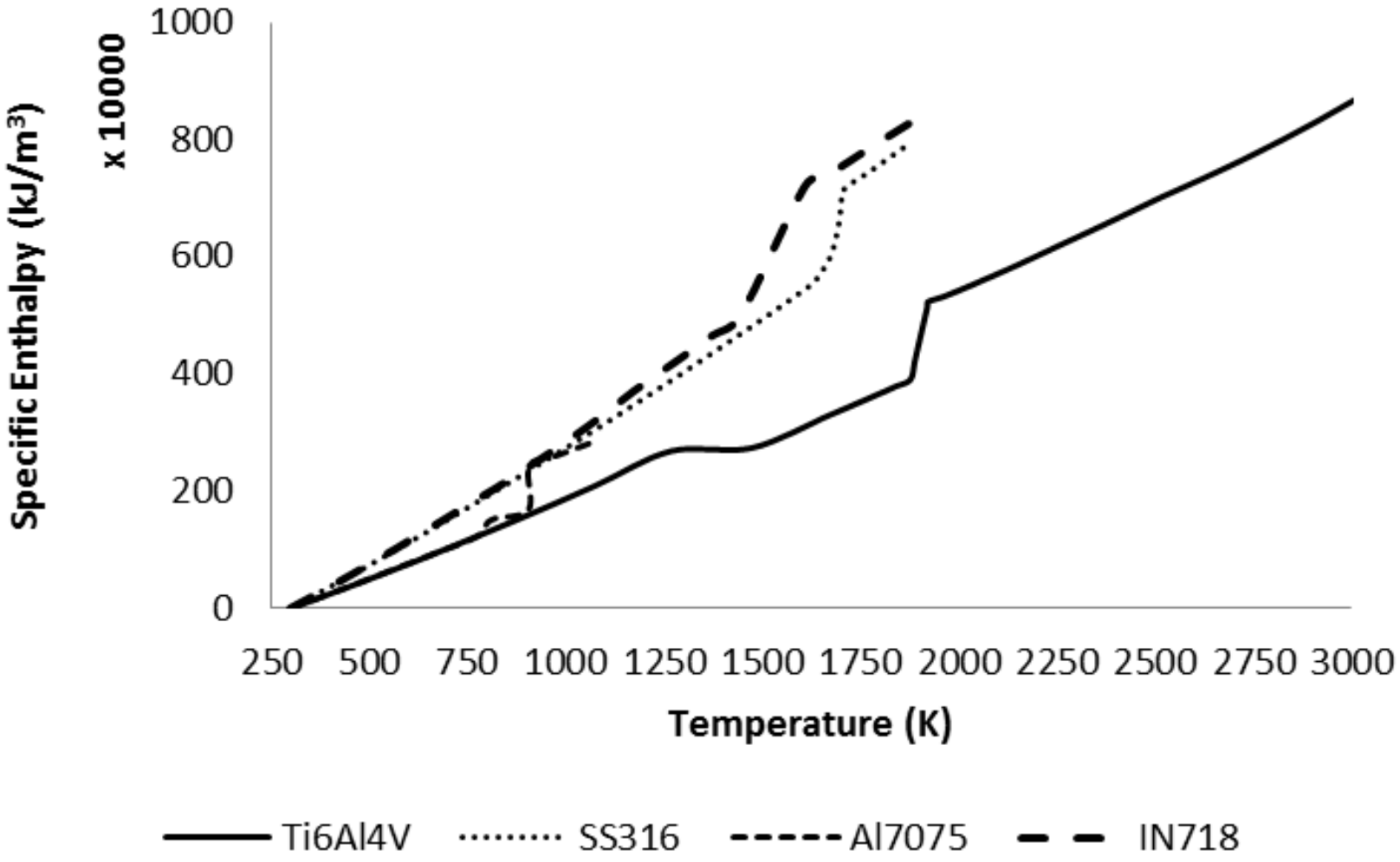
Specific Enthalpy (kJ/m³)
x 10000
1000
800
600
400
200
0
250 500 750 1000 1250 1500 1750 2000 2250 2500 2750 3000
Temperature (K)
Ti6Al4V
SS316
Al7075
IN718

[38], [50]

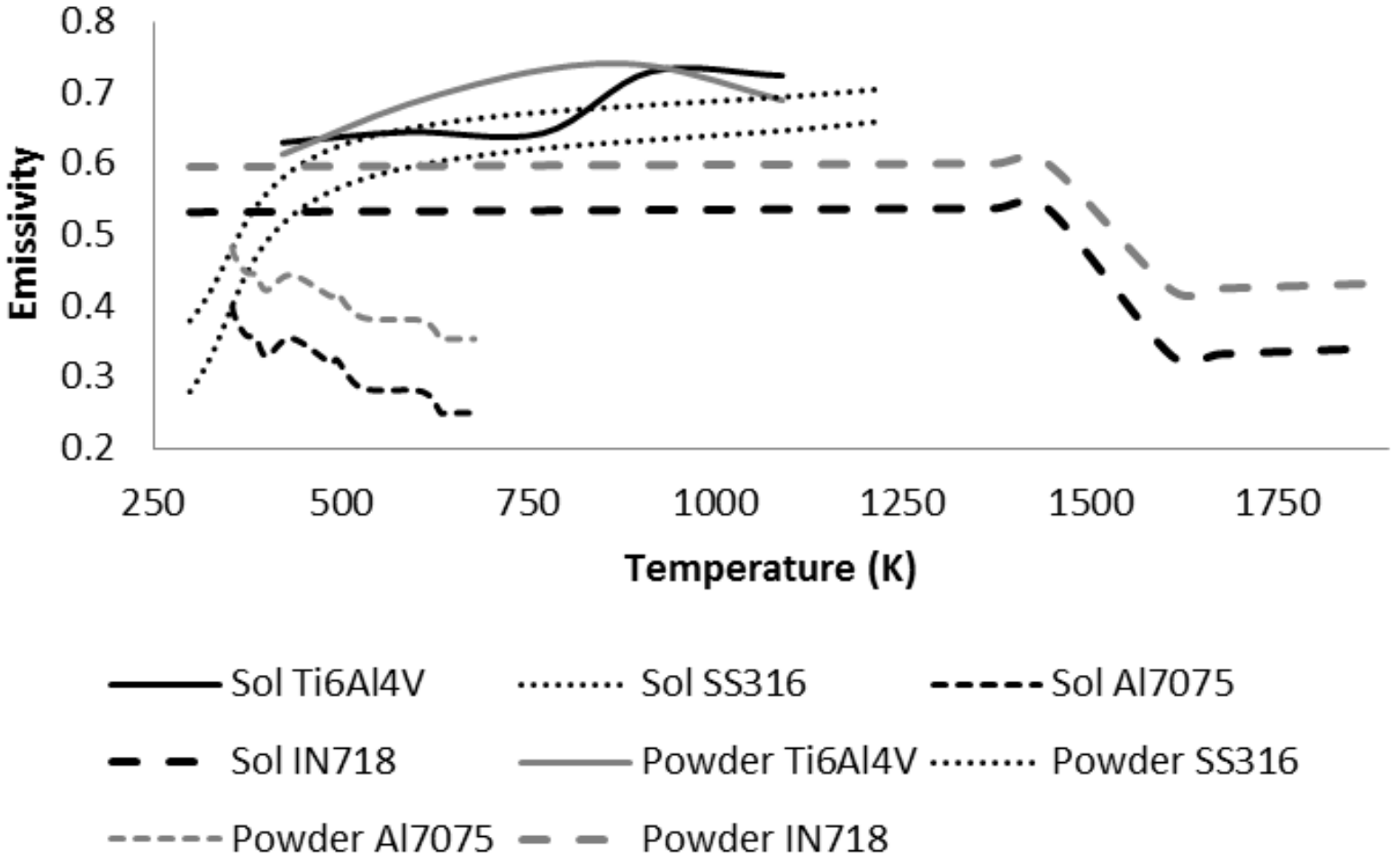
0.8
0.7
0.6
0.5
0.4
0.3
0.2
Emissivity
250
500
750
1000
1250
1500
1750
Temperature (K)
Sol Ti6Al4V
Sol SS316
Sol Al7075
Sol IN718
Powder Ti6Al4V
Powder SS316
Powder Al7075
Powder IN718

[27], [38]

APPENDIX C: Glossary of Symbols:

a, A_1, A_2, A_3	*Various Scaling Constants*
c	*Specific Heat*
e	*Specific Internal Energy*
g	*Acceleration of Gravity*
h	*Convective Heat Transfer Coefficient*
k	*Thermal Conductivity*
k_e	*Effective Powder Thermal Conductivity*
k_{eff}	*Effective Liquid Thermal Conductivity*
k_g	*Void Fluid Thermal Conductivity*
k_s	*Bulk Solid Thermal Conductivity*
L	*Characteristic Length*
q''	*Heat Flux (heat input per area)*
q'''	*Heat Generation (heat input per volume)*
T	*Temperature*
T_∞	*Far Field Temperature*
T_{liq}	*Liquidus Temperature*
T_m	*Theoretical Maximum Temperature*
T_{sol}	*Solidus Temperature*
v	*Fluid Velocity*
v_{scan}	*Beam Scan Speed*
V	*Melt Pool Volume*
$\dot{W}$	*Beam Power Input*
X	*A Generalized Body Force*
x,y,z	*Model Coordinates*
x_c,y_c	*Beam Center Coordinates*
α	*Spectral Absorptivity*
γ	*Surface Tension*
δ	*Beam Penetration Depth*
ΔT	*Change in Temperature between* T_m *and* T_{sol}
ε	*Spectral Emissivity*
η	*Powder Bed Porosity*
ν	*Kinematic Viscosity*
ρ	*Density*
σ	*Stefan-Boltzmann Constant* ($5.67x10^{13}\ \frac{W}{m^2K^4}$)
τ	*Stress Tensor (hydrostatic and deviatoric stresses)*
Φ	*Effective Beam Diameter*
$\frac{D}{Dt}$	*Material Derivative*
∇	*Gradient Operator*

APPENDIX D: Glossary of Abbreviations:

Al	*Aluminum*
APDL	*ANSYS Program Design Language*
CAD	*Computer Aided Design*
CFD	*Computational Fluid Dynamics*
DMLS	*Direct Metal Laser Sintering*
EBM	*Electron Beam Melting*
FDM	*Fused Deposition Modeling*
FEM	*Finite Element Modeling*
IJP	*Ink Jet Printing*
IN	*Inconel*
LENS	*Laser Engineered Net Shaping*
LOM	*Laminated Object Manufacturing*
SLM	*Selective Laser Melting*
SLS	*Selective Laser Sintering*
SS	*Stainless Steel*
STL	*Standard Tessellation Language/Stereolithography*
Ti	*Titanium*
V	*Vanadium*
Bo	*Bond Number – comparing buoyant force to surface tension force*
Ma	*Marangoni Number – comparing surface tension force to viscous force*
Nu	*Nusselt Number – comparing convective to conductive heat transport*